UHASSELT

KNOWLEDGE IN ACTION

Faculteit Wetenschappen

master in materiomics

Masterthesis

Linearizing the Electrical Readout of NV Centers in Diamond Using a Thin B-doped Layer

Nathan Deveux

Scriptie ingediend tot het behalen van de graad van master in materiomics

PROMOTOR :

Prof. dr. Milos NESLADEK

2024
2025

UHASSELT

KNOWLEDGE IN ACTION

www.uhasselt.be
Universiteit Hasselt
Campus Hasselt:
Martelarenlaan 42 | 3500 Hasselt
Campus Diepenbeek:
Agoralaan Gebouw D | 3590 Diepenbeek

UHASSELT

KNOWLEDGE IN ACTION

Faculteit Wetenschappen

master in materiomics

Masterthesis

Linearizing the Electrical Readout of NV Centers in Diamond Using a Thin B-doped Layer

Nathan Deveux

Scriptie ingediend tot het behalen van de graad van master in materiomics

PROMOTOR :

Prof. dr. Milos NESLADEK

Table of Contents

Linearizing the Electrical Readout of NV^- Centers in Diamond Using a Thin B-doped Layer

Nathan Deveux[1,], Remy Vandebosch[2], Eddy Kunnen[2], Emilie Bourgeois[2,3] & Milos Nesladek[2,3]*

[1] Hasselt University, Martelarenlaan 42, 3500 Hasselt, Belgium
[2] Institute for Materials Research (IMO), Hasselt University, Wetenschapspark 1, 3590 Diepenbeek, Belgium
[3] IMOMEC division, IMEC, Wetenschapspark 1, 3590 Diepenbeek, Belgium
E-mail: nathan.deveux@student.uhasselt.be

Keywords: back-to-back Schottky, ohmic, electrodes, B-doped, NV^- center, diamond

Abstract: Photoelectric detection of magnetic resonance (PDMR) catches photogenerated electrons from negatively charged nitrogen-vacancy (NV^-) centers in diamond, enabling electron spin readout for quantum computing and sensing applications. These electrons are captured by metal electrodes patterned on a single-crystal diamond slab under an external electric field. However, conventional electrodes exhibit back-to-back Schottky diodes behavior, which is a suboptimal configuration for the collection of photogenerated electrons.

To overcome this limitation, electrodes, approaching ohmic-like current response more closely, are fabricated by introducing a thin B-doped diamond layer, followed by Ti/Al bilayer metallization via RF sputtering. Both the diamond slab containing NV^- centers and the B-doped layer are grown with microwave plasma-enhanced chemical vapor deposition. The B-doped layer between the electrodes is selectively etched, ensuring current flows only through the buried B-doped layer within the electrodes.

Fabricated electrodes show improvement with respect to ohmic current response on the *I-V* characteristic. Quantum tunneling is discussed as possible contributing transport mechanism at the metal/diamond interface. The photoelectric gain γ is estimated between 10 and 400, indicating improved performance over conventional electrodes with a photoelectric gain γ between 1 and 40, thereby demonstrating enhanced performance for PDMR-based quantum applications.

Abstract: Foto-elektrische detectie van magnetische resonantie (PDMR) vangt uitgezonden elektronen op uit negatief geladen stikstof-gatcentra (NV^-) in diamant, waardoor elektronen-spinuitlezing mogelijk wordt voor kwantumcomputer en -sensortoepassingen. Deze elektronen worden opgevangen door metalen elektroden, gedeponeerd op een diamanten substraat, onder een extern elektrisch veld. Conventionele elektroden vertonen echter back-to-back Schottky diodengedrag, wat een suboptimale configuratie is voor het verzamelen van fotogegenereerde elektronen.

Om deze beperking te overwinnen, worden elektroden, die dichter bij het ohmse gedrag komen, vervaardigd door het introduceren van een dunne, met een B-gedoteerde diamantlaag, gevolgd door Ti/Al dubbellaagse metallisatie via RF-sputteren. Zowel het diamanten substraat met NV^--centra als de B-gedoteerde laag zijn gegroeid met microgolfplasma-versterkte chemische dampafzetting. De B-gedoteerde laag tussen de elektroden wordt selectief geëtst, waardoor de stroom alleen door de ingebedde B-gedoteerde laag binnen de elektroden vloeit.

Gefabriceerde elektrodes tonen verbetering met betrekking tot ohms gedrag op de *I-V* karakteristiek. *Quantum tunneling* is besproken als mogelijk bijdragend transportmechanisme op het metaal/diamanten grensvlak. De foto-elektrische versterking γ wordt geschat tussen 10 en 400, wat een verbetering vertegenwoordigt ten opzichte van conventionele elektroden met een foto-elektrische versterking γ tussen 1 en 40, waardoor verbeterde prestaties voor op PDMR-gebaseerde kwantumtoepassingen worden aangetoond.

1 Introduction

Over the last two decades, the negatively charged nitrogen-vacancy (NV^-) center, engineered in the diamond lattice, has been essential for quantum computing and sensing applications.[1–6] These applications face challenges such as quantum decoherence[7,8], positioning of the centers[9] and efficient readout[10]. Typically used optical readout techniques are limited by the low collection efficiency of photons due to the limitations of objective optics and diamond's high refraction index, resulting in a large number of detection repetitions to achieve good photon statistics for single spin readout.[10,11] In addition, the saturation of the photon flux is determined by the short lifetime of the NV^- excited state. In 2015, photoelectric detection of magnetic resonance (PDMR) emerged as a promising readout technique for the NV^- center's electron spin state.[12] PDMR leverages the principles of optical spin polarization of NV^- electronic states with subsequent spin dependent photoionization of the electron to the conduction band and electrically detected magnetic resonances.[13]

The NV^- center consists of a nearest-neighbor pair of a substitutional nitrogen atom and a lattice vacancy, incorporating an extra electron. The diamond color center hosts six electrons: two from the nitrogen doublet and the extra electron forms a spin S=1 pair with one of the three electrons of the dangling bonds of the carbon atoms surrounding the lattice vacancy. The NV^- center is popular for its long spin coherence time at room temperature and unique electronic structure, which includes a spin-triplet ground state, spin-triplet excited state and two spin-singlet states between the valence and conduction band. Green laser light (wavelength of $\approx$ 532 nm, photon energy of $\approx$ 2.33 eV) optically pumps the NV^- center in the $|0\rangle$ sublevel of the spin-triplet ground state, while simultaneously promoting an electron through sequential two-photon absorption from the ground state to the excited state and then to the conduction band, resulting in ionization to the neutral NV^0 state. This process is known as two-photon ionization. The NV^- configuration is recovered via two-photon back-conversion, where the first absorbed photon excites an electron from the spin-triplet ground state to the spin-triplet excited state and the second absorbed photon excites an electron from the valence band to the spin-triplet ground state, producing a hole in the valence band and generating a measurable photocurrent. A resonant microwave (MW) field of 2.87 GHz causes a repopulation of the $|0\rangle$ and $|\pm1\rangle$ spin sublevels. Electrons from both spin sublevels may undergo photoionization, but due to the preference of $|\pm1\rangle$ states for faster non-radiatively decay through the singlet states, known as

intersystem crossing (ISC), $|0\rangle$ states are more likely to be ionized because they exhibit longer excited state lifetimes. Consequently, depopulation of the $|0\rangle$ state reduces the photocurrent, enabling spin state detection via the PDMR signal. **(Figure 1b)** In other words, the spin dependence of the ISC enables the spin contrast detection in the PDMR signal.[13] In PDMR, the saturation is limited by the charge carrier recombination lifetime, which is several orders of magnitude higher than the short lifetime of the NV^- excited state. The PDMR technique enables enhanced detection rates, boosting the sensitivity of NV-based sensors. It is scalable, compatible with modern lithographical chip manufacturing and an all-diamond single-material device application.[13] PDMR collects the NV^--emitted electrons from photoionization in an external electrical circuit by applying a bias voltage between coplanar electrodes creating an electric field under which the electrons can travel freely to the electrodes.[14] **(Figure 1a)** The NV^- centers are positioned between and underneath the electrodes, which are lithographically deposited on a diamond slap holding the NV^- centers. PDMR still requires further research on the optical polarization of NV^- electron spin, NV center excitation and photoionization, as well as the charge carrier transport.[13]

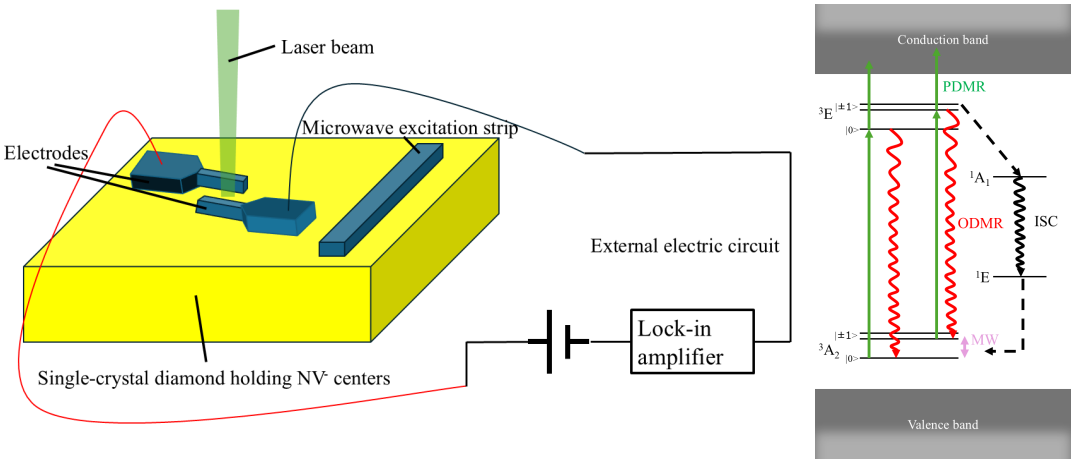

(a) **(b)**

Figure 1. (a) Schematic representation of the PDMR setup. (b) NV^- electronic structure and schematic representation of the ODMR and PDMR mechanisms.

The electrodes play a crucial role in the charge carrier transport. Currently, the electrodes exhibit back-to-back Schottky diodes behavior. They are blocking current until the applied voltage is high enough for the junction to leak current as breakdown approaches.[14] In the back-to-back Schottky diodes configuration, two Schottky electrodes are connected back-to-back with a series resistance in between them.[15] At each metal-semiconductor interface, a space charge

region forms, creating a potential barrier that hinders carrier flow.[16] These barriers limit quantum tunneling or thermionic field emission, restricting current flow at low biases.[16] Beyond this ohmic-like region, current increases exponentially when one barrier begins to conduct.[15] However, the reverse-biased electrode continues to impede carrier extraction, increasing residence time and enhancing recombination probabilities.[16] This renders the back-to-back Schottky diodes configuration suboptimal for collecting the photogenerated charge carriers. In contrast, ohmic electrodes solve this limiting current response, allowing effective extraction of electrical current. In general, an electrode is ohmic if the *I*-*V* relationship under both the reverse and forward bias conditions is linear.[17] However, a metal-semiconductor electrode is ohmic if it has a negligible contact resistance relative to the bulk or series resistance of the semiconductor. It can pass current with a voltage drop across the metal-semiconductor interface, which is small compared to the voltage drop across the bulk semiconductor.[16,17] Quantum tunneling or thermionic field emission is the dominant phenomenon behind ohmic behavior, especially in doped semiconductors. It combines thermionic emission and quantum tunneling. In thermionic emission, charge carriers gain enough thermal energy to surmount the potential barrier of the metal-semiconductor interface and even be thermionically emitted into the vacuum. Before this happens, the charge carrier wave function penetrates the potential barrier after being thermally excited to an energy where this becomes possible. Now, charge carriers can tunnel through the remaining thinner portion of the potential barrier.[16]

A major challenge in diamond-based semiconductor devices, including the PDMR setup, is the fabrication of low-resistance ohmic electrodes. The formation of these electrodes is critical because they determine the efficiency of charge carrier transport and influence overall device performance. Due to the large band gap[18,19] of the diamond, defining it as a wide-band gap semiconductor, and its chemical inertness[20,21], achieving reliable ohmic behavior at the metal-diamond interfaces remains a fundamental issue in diamond electronics. One widely explored approach involves heavy boron doping, which narrows the Schottky barrier width, thereby promoting tunneling conduction and reducing contact resistivity resulting in ohmic behavior.[18,21] B-doped diamond is a p-type semiconductor and diamond containing NV^- centers is a n-type semiconductor, forming a p-n junction. When boron concentrations exceed 10^{20} cm^{-3}, the depletion region at the metal-diamond interface becomes sufficiently thin ($\approx$ 5 nm), allowing for efficient carrier injection depending on the strength of the electric field.[22,23] However, the effectiveness of this doping strategy is highly sensitive to implantation depth, annealing condi-

tions, and surface termination effects. An alternative and often complementary method involves the use of carbide-forming metals such as Ti[19,21,24–26], Mo[19,21,26,27], Ta[25,26] and W[26]. These metals exhibit strong chemical affinities for carbon, forming stable interfacial carbides that lower the Schottky barrier height[20,21,26] and improve adhesion[27]. Annealing at temperatures above approximately 400 °C[20,21,24–27] facilitates carbide formation, thus significantly reducing contact resistance. However, precise control of annealing parameters is required to prevent unwanted structural modifications such as diamond amorphization and graphitization[28,29] or metallic phase changes[25,30], which can degrade electrical performance. In addition to doping and carbide formation, surface termination plays a crucial role in determining electrode properties. Hydrogen termination of p-type diamond leads to a surface conductivity that can vary by several orders of magnitude depending on environmental conditions[31], making it less stable for long-term device operation[32]. In contrast, oxidation of the diamond surface typically results in strong Fermi level pinning, which can hinder charge injection.[33] Recent studies[34,35] suggest that selective oxidation, in which only the electrode regions retain hydrogen termination while the surrounding areas are oxidized, can improve device stability while maintaining low contact resistivity. Regardless of the surface termination, Ti-based electrodes remain widely used because of their ability to form titanium carbide at moderate annealing temperatures, also for B-doped diamond films.

Despite these advancements, several unresolved issues remain in the pursuit of ideal ohmic electrodes to diamond. The low diffusivity of diamond dopants complicates traditional ion implantation methods, which require high-temperature annealing to activate boron atoms and repair damage caused by implantation.[28,36] Uncontrolled oxygen contamination during annealing is another concern, as it can hinder carbide formation and increase the Schottky barrier height.[21,37] Moreover, while carbide-forming metals are effective in reducing contact resistance, the exact mechanisms by which they influence electronic transport are still being investigated. Further research is required to systematically study the interplay between doping concentration, surface preparation, metallization choice, and thermal processing conditions to develop stable, reproducible, and low-resistance ohmic electrodes for diamond-based semiconductor devices. In this study, Al/Ti/B-doped diamond electrodes to diamond holding NV^- centers have been fabricated. The performance of the fabricated electrodes is determined by their specific contact resistance ρ_c and transfer length L_T, measured using the transfer length method (TLM), the external quantum efficiency *EQE* and the photoelectric gain γ. The deviant behavior of the

back-to-back Schottky diodes configuration is observed in *I-V* characteristics. The paper proceeds as follows: section 2 discusses research results; section 3 addresses the interdisciplinary nature of the research and sustainability related to the research; section 4 concludes the paper; and finally, section 5 presents an overview of the experimental procedures along with the used materials and laboratory equipment. It is recommended to start with experimental section 5 to process the flow of this work.

2 Results and Discussion

To evaluate the fabricated electrodes, *I-V* characteristics were measured. **Figure 2** shows the *I-V* characteristics of four fabricated electrode pairs, two on sample A and two on sample B, with various spacings and illumination powers. The photocurrent in figure 2 is in logarithmic scale for detailed electrode configuration analysis. **Figure 2a and 2b** of sample A are typical *I-V* characteristics of back-to-back Schottky diodes configuration electrodes, but with a small deviation. In fact, there is a linear part at lower bias voltages (as can be seen in **figure S5b and S5e and figure S6c and S6d**). This linear portion is often fitted by the charge carrier tunneling mechanism[38,39]. The adapted model of Milazzo et al.[40] is used here:

$$I = A \cdot e \cdot D \cdot \upsilon_D \cdot exp(-\frac{\Phi_B - \mu_n}{E_0}) \cdot exp(\frac{e \cdot V}{E_0}), \tag{1}$$

where *A* is the electrode surface, *e* is the elementary charge (1.602x10^{-19} C), *D* is the dislocation density, υ_D is the Debye frequency, Φ_B is the effective Schottky barrier height, μ_n is the chemical potential, E_0 is the tunneling parameter and *V* is the applied bias voltage. In wide-band gap semiconductors like diamond, the chemical potential μ_n indicates the energy level at which the probability of finding an electron is 50%. For undoped semiconductors, this level typically lies near the center of the band gap. Doping of the material shifts the chemical potential μ_n. In N-doped diamond, nitrogen atoms introduce donor levels deep within the band gap, approximately 1.7 eV below the conduction band minimum. This deep donor level corresponds to the activation energy required to excite an electron into the conduction band. Consequently, the chemical potential aligns near this donor level, reflecting the energy necessary for electrical conduction in the doped diamond.[41] E_0 is the energy corresponding to the maximum tunneling

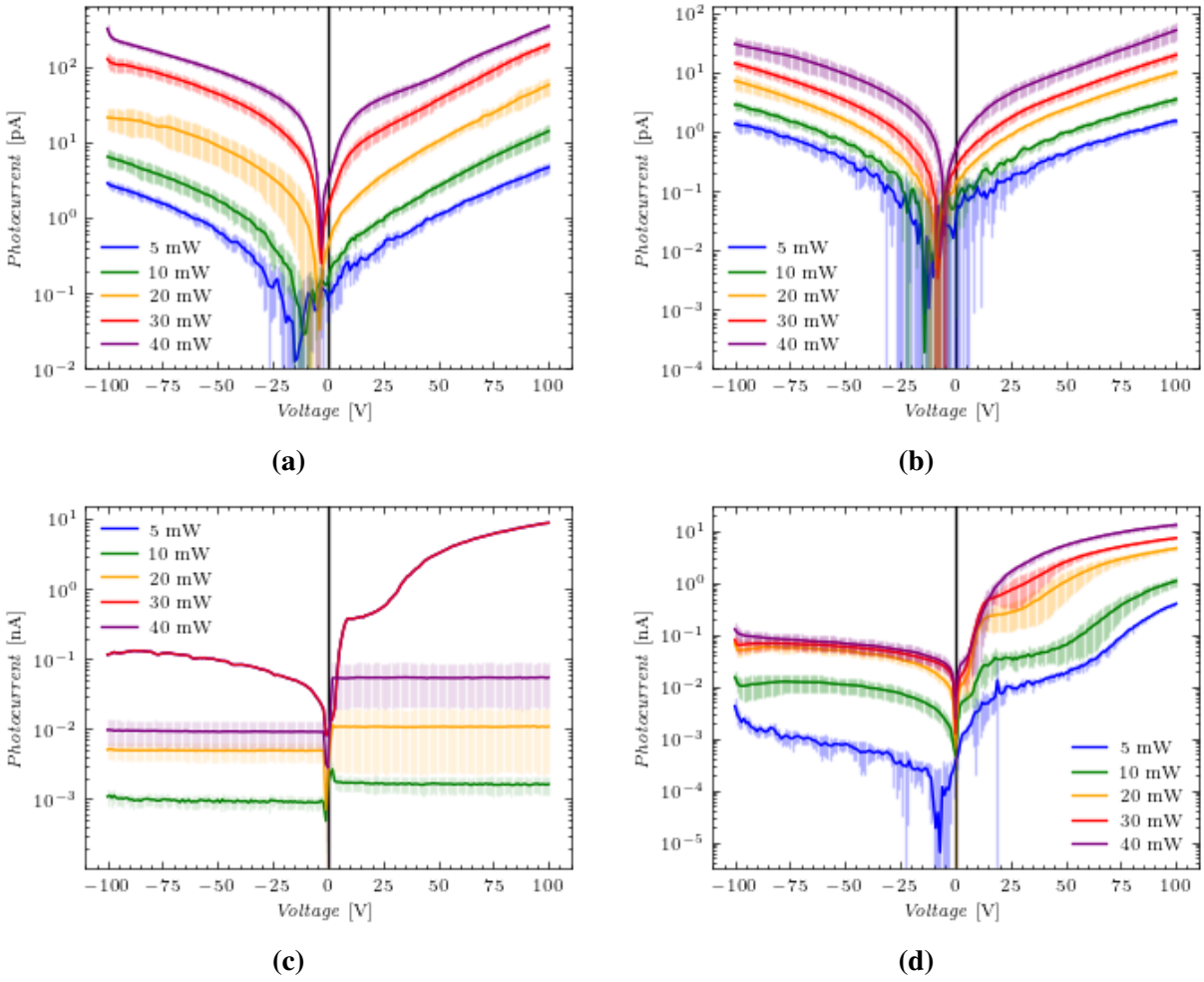

Figure 2. *I-V* characteristic of the average photocurrent, over 10 measurements, as a function of applied voltage at different laser powers, obtained for (a) sample A with an electrode spacing of 5 μm, (b) sample A with an electrode spacing of 7.5 μm, (c) sample B with an electrode spacing of 5 μm and (d) sample B with an electrode spacing of 15 μm. The error bars are the standard deviation of the 10 measurements. The *I-V* characteristics at 5 and 10 mW for subfigure (c) coincide and are a single measurement with no error bars for display reasons.

probability through a barrier[16], expressed as:

$$E_0 = E_{00} \cdot coth(\frac{E_{00}}{k_B \cdot T}), \tag{2}$$

where E_{00} is the characteristic tunneling energy related to the tunnel effect transmission probability[42], k_B is the Boltzmann's constant (1.381×10^{-23} $m^2 kg s^{-2} K^{-1}$) and T is the absolute temperature. After the linear portion, the current grows exponentially. This region can be described by thermionic emission theory[16]:

$$I = A \cdot A^* \cdot T^2 \cdot exp(-\frac{e \cdot \Phi_B}{k_B \cdot T}) \cdot exp(\frac{e \cdot V}{n \cdot k_B \cdot T}), \tag{3}$$

where A is the electrode surface, A^* is the Richardson constant for the electrode-limiting interface, T is the absolute temperature, e is the elementary charge, Φ_B is the total effective Schottky barrier height, k_B is the Boltzmann's constant, V is the applied bias voltage and n is the ideality factor. The two regions are connected through the correlation between tunneling parameter E_0 and ideality factor n[43]:

$$E_0 = n \cdot k_B \cdot T. \tag{4}$$

Each polarity of each *I-V* characteristic of figure 2a and 2b was fitted with a simplified model, over an entire positive/negative voltage sweep or over a small voltage window at low bias, representing exponential growth:

$$I_{ph}(V) = a/c \cdot sinh(b/d \cdot V), \tag{5}$$

where I_{ph} is the photocurrent, V is the applied bias voltage, a is a pre-factor and b is a scaling factor for the case of the entire positive/negative voltage sweep and c is a pre-factor and d is a scaling factor for the case of a small voltage window at low bias. The use of separate fittings for each polarity is justified since each half represents a different forward/reverse configuration of the diodes with the caveat that the injected charge carriers into the junction in reverse bias change the charge carrier concentration, e.g. holes, causing excess majority carriers at high voltages. This simplification represents one electrode as ohmic in forward bias, while the other is the limiting electrode in reverse bias. Equation (5) effectively describes the exponential behavior of each polarity individually, validating that the configuration has no intrinsic polarity, i.e. symmetry, which is characteristic of two Schottky barriers in series. From equation (1)

follows that pre-factor *c* and scaling factor *d* equal:

$$c = \frac{A \cdot e \cdot D \cdot v_D}{2} \cdot exp(-\frac{\Phi_B - \mu_n}{E_0}); \tag{6}$$

$$d = \frac{e}{E_0}, \tag{7}$$

for the linear portion. From equation (3) follows that pre-factor *a* and scaling factor *b* equal:

$$a = \frac{A \cdot A^* \cdot T^2}{2} \cdot exp(-\frac{e \cdot \Phi_B}{k_B \cdot T}); \tag{8}$$

$$b = \frac{e}{n \cdot k_B \cdot T}, \tag{9}$$

for the exponential portion. **Figure 3** shows a fit by equation (5) on the positive voltage sweep of the *I-V* characteristic of the electrode pair of figure 2b at a laser power of 20 mW. The red dash-dot line represents the linear region, while the blue dashed line represents the exponential region. Following equation (8) and (9) and for an electrode surface *A* of 7.5x10^{-14} m^2, an

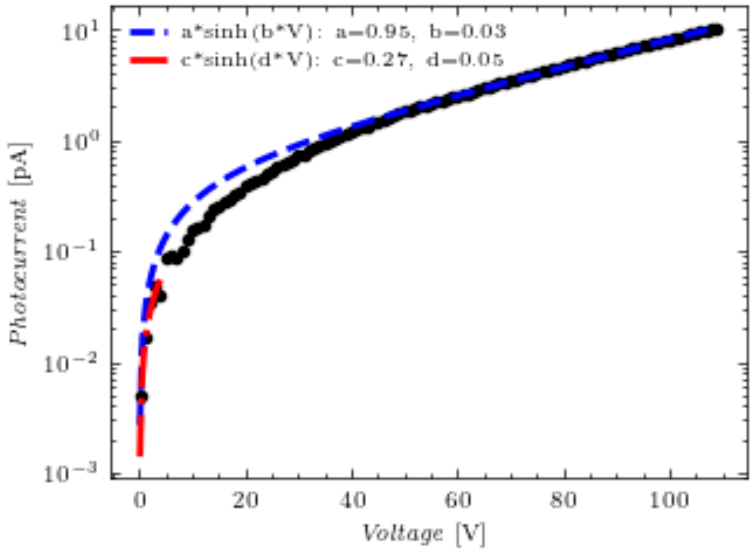

Figure 3. Fit of the *I-V* characteristic of the average photocurrent, over 10 measurements, as a function of the positive applied voltage sweep at a laser power of 20 mW obtained for sample A with an electrode spacing of 7.5 μm, by fitting model $I_{ph}(V) = a \cdot sinh(b \cdot V)$ over the full positive voltage sweep and $I_{ph}(V) = c \cdot sinh(d \cdot V)$ over a voltage window at low bias. The dark blue dashed line represents the exponential region of the *I-V* characteristic, and the red dash-dot line represents the linear region of the *I-V* characteristic.

absolute temperature *T* of 300 K and a Richardson constant A^* of 9x10^5 Am^{-2}K^{-2}[44], ideality factor *n* equals 1, 000 and the effective Schottky barrier height Φ_B equals 0.09 eV for the electrode of figure 3. From the relation of equation (4) it follows that the tunneling parameter

E_0 equals 40 eV. Following equation (6) and (7) and for an electrode surface A of 7.5x10^{-14} m^2, a dislocation density D of 4x10^6 m^{-2}[45], a Debye frequency of 39.39x10^{13} rad/s, a chemical potential μ_n of 1.7 eV[46] and an absolute temperature T of 300 K, tunneling parameter E_0 equals 20 eV and the effective Schottky barrier height Φ_B equals -300 eV for the electrode of figure 3. The large discrepancy between the two values for the effective Schottky barrier height Φ_B indicates a failure of the applied models and a large underestimation of the effective Schottky barrier height Φ_B by the tunneling model. In addition, the non-physical values for both the ideality factor n extracted in the exponential region and the effective Schottky barrier height Φ_B extracted in the linear region, as also mentioned in the previous sentence, indicate that the fitting model in equation (5) is completely wrong. Temperature dependent measurements at lower voltage biases are necessary to discover which physical mechanisms are actually at play and to what extent in the charge carrier conduction by the fabricated electrodes on sample A.[40] Only in this way will the chosen models from Milazzo et al.[40] be correctly applied to this work. Furthermore, effects such as barrier inhomogeneities, interface states, or series resistance may further distort the apparent parameters extracted using idealized models.[47–49] A better approach would be to use a back-to-back Schottky diodes configuration with two different ideality factors and a series resistor[15]:

$$V = \frac{n_1 \cdot k_B \cdot T}{e} \cdot ln(\frac{J}{J_{01}} + 1) - \frac{n_2 \cdot k_B \cdot T}{e} \cdot ln(\frac{J}{J_{02}} + 1) + R \cdot A \cdot J, \tag{10}$$

where V is the applied bias voltage, n_1 is the ideality factor of the first Schottky diode, k_B is the Boltzmann's constant, T is the absolute temperature, e is the elementary charge, J is the current density in the back-to-back Schottky diodes, J_{01} is the saturation current density in the first Schottky diode, n_2 is the ideality factor of the second Schottky diode, J_{02} is the saturation current density in the second Schottky diode, R is the series resistance and A is the contact area. In figure 2a and 2b, a higher leakage current can be observed than in standard back-to-back Schottky diodes. Leakage current in a Schottky diode refers to the small current that flows through the diode even when it is reverse biased, i.e. when it is supposed to block current flow. Thermionic field emission or charge carrier tunneling directly contributes to this increased leakage current by allowing electrons to quantum-mechanically pass through the Schottky barrier even when the diode is reverse biased.[50–52] Hence, the model of Mikhelashvili et al.[53] is even more suitable

to explain the *I-V* characteristics of this work:

$$J_T = \frac{2 \cdot J_{s1} \cdot J_{s2} \cdot sinh(\frac{e \cdot V}{2 \cdot k_B \cdot T})}{J_{s1} \cdot exp(\frac{e \cdot V}{2 \cdot k_B \cdot T}) + J_{s2} \cdot exp(-\frac{e \cdot V}{2 \cdot k_B \cdot T})}, \tag{11}$$

where J_T is the total current density, J_{s1} is the leakage current density through the first reverse-biased Schottky junction, J_{s2} is the leakage current density through the second reverse-biased Schottky junction, e is the elementary charge, V is the applied bias voltage, k_B is the Boltzmann's constant and T is the absolute temperature. When the electrode in forward bias is considered ohmic, the electrode in reverse bias can still be fitted with the model of equation (5), after each *I-V* characteristic has been split by polarity, and thus can be linked to model (11).

Figure 2c and 2d of sample B displays two types of *I-V* characteristic, where each type can be observed on the same electrode pair for different optical powers. One type relates to photoconductor behavior, while the other relates to space charge limited current (SCLC). **Figure 4a** is a typical *I-V* characteristic of a photoconductive response of a metal-semiconductor electrode[54–57], wherein excess minority electrons are excited to the conduction band in the semiconductor and no excess electrons will be generated in the metal upon illumination.[58] The B-doped diamond is the semiconductor in contact with the metal and receiving the photogenerated electrons from the N-doped diamond. The B-doped diamond is doped with acceptor atoms, leaving holes as majority carriers and electrons as minority carriers. The excess minority carrier spatial distribution is symmetric and zero at the metal-semiconductor interface, resulting in excess electrons in the semiconductor diffusing toward the metal. At zero voltage, there is no net photocurrent flow. At nonzero voltage, the spatial distribution of photogenerated excess minority carriers is skewed by the electric field, creating net photocurrent. At low voltage (i.e. small electric field), the transit time $t_{transit}$ is significantly longer than the recombination lifetime τ, leaving the spatial distribution of photogenerated excess minority carriers relatively uniform in the semiconductor. At a certain voltage (i.e. increased electric field), the skewing of the spatial distribution of photogenerated excess minority carriers reaches a maximum, causing the photocurrent to saturate.[58] Different polarities of the *I-V* characteristics of figure 2c and 2d that exhibit a photoconductive response, were fitted with the phenomenological model:

$$I_{ph}(V) = a \cdot tanh(\frac{V}{b}), \tag{12}$$

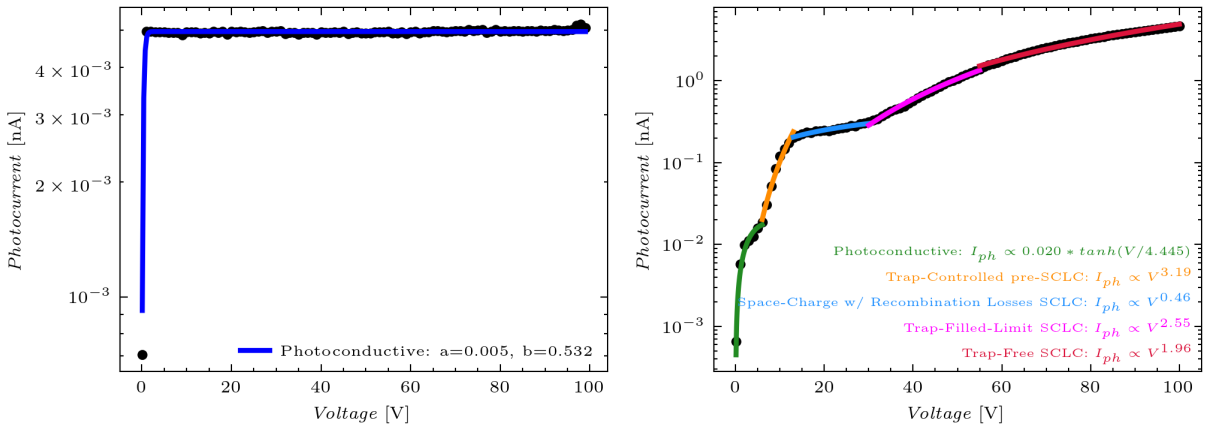

(a) **(b)**

Figure 4. Fit of the *I-V* characteristic of the average photocurrent, over 10 measurements, (a) as a function of the negative applied voltage sweep at a laser power of 20 mW obtained for sample B with an electrode spacing of 5 μm, by fitting model $I_{ph}(V) = a \cdot tanh(\frac{V}{b})$ in the dark blue line representing photoconductive behavior and, (b) as a function of the positive applied voltage sweep at a laser power of 20 mW obtained for sample B with an electrode spacing of 15 μm, by fitting model $I_{ph}(V) = a \cdot tanh(\frac{V}{b})$ in the green line representing photoconductive behavior and $I_{ph}(V) = V^x$ in the orange line representing trap-controlled pre-space charge limited current (SCLC), in the light blue line representing space-charge conduction with surface or interface recombination losses, in the pink line representing trap-filled SCLC and in the red line trap-free SCLC.

so that pre-factor a is the point where the photocurrent saturates and scaling factor b is the voltage window over which the photocurrent transitions to saturation. For the electrode of figure 4a the photocurrent saturates at 5.0 $\pm$ 1.1 pA and takes a voltage window of 0.5 V to transition to saturation. The smaller this voltage window, the longer the minority carrier recombination lifetime τ. The saturation photocurrent is[58]:

$$I_{sat} = e \cdot g_n \cdot L, \tag{13}$$

where e is the elementary charge, g_n is the generation rate of minority electrons and L is the electrode spacing. At large electric fields, the diffusion length is no longer much smaller than the device length L. For a saturation photocurrent I_{sat} of 5.0 $\pm$ 1.1 pA and an electrode spacing L of 5x10^{-4} cm, the electrode of figure 4a has a generation rate of minority electrons g_n of 6.1877x10^{10} $\pm$ 1.4262x10^{10} cm^{-3}s^{-1}. Therefore, the level at which the photocurrent saturates is dictated by the optical power determining the generation rate of minority electrons g_n. This explains increasing levels of saturating photocurrent with increasing optical power in figure 2c.

At a small electric field, the photocurrent is[58]:

$$I_{ph} = e \cdot g_n \cdot \tau_n \cdot \mu_n \cdot V, \tag{14}$$

where *e* is the elementary charge, g_n is the generation rate of minority electrons, τ_n is the minority carrier recombination lifetime, μ_n is the minority electron mobility and *V* is the voltage bias applying the electric field. For the electrode of figure 4a, with an assumed electron mobility μ of 3.6x10^2 cm^{2}V^{-1}s^{-1}[59] and regarding the first point of the saturation photocurrent on the voltage scale, the minority carrier recombination lifetime τ_n is 2.6111 $\pm$ 0.6018 μs. The lower magnitude of the photocurrent for negative voltage sweeps in figure 2c and 2d is thought to be caused by the recombination of photocarriers and a large threshold voltage of this device.[57] Photocarriers travel to the electrodes by diffusion but also by drift in the presence of electric field.[57] Nevertheless, photocarriers generated outside the depletion region of the metal-semiconductor junction are not efficiently extracted due to recombination/trapping by crystal defects, surface states and the surface depletion region.[57,58]

Figure 4b is an uncommon *I*-*V* characteristic for a metal-semiconductor electrode. In order to evaluate the different regimes of the photocurrent response, the *I*-*V* characteristic was segmented, where each segment is fitted with an explanatory model, as seen in figure 4b. The first segment is fitted with equation (12), dedicating it to the previously described photoconductive response of a metal-semiconductor interface. The steep rise in photocurrent observed in the second segment is attributed to trap-controlled injection, where carriers begin to fill exponentially distributed traps.[60–62] This second segment exhibits following relation[62]:

$$I_{ph} \propto V^{(\frac{T_c}{T}+1)}, \tag{15}$$

where T_c is the characteristic temperature of the trap distribution and *T* is the absolute temperature. Assuming that the absolute temperature *T* is 300 K, the characteristic temperature of the exponential trap distribution T_c is around 657 K for the electrode of figure 4b. As the trap population saturates, the system transitions into a recombination-dominated regime (segment 3), where space-charge buildup is accompanied by significant surface or interface recombination, effectively suppressing the current increase and yielding a sublinear *I*-*V* behavior.[63] Accompanied with an imbalance between the minority and majority carrier mobilities, the derived

expression for sublinear space-charge photoconduction is[64,65]:

$$I_{ph} = (\frac{9}{8} \cdot \epsilon \cdot \mu_{slow})^{\frac{1}{4}} \cdot (e \cdot G)^{\frac{3}{4}} \cdot V^{\frac{1}{2}}, \tag{16}$$

where ϵ is the dielectric constant, μ_{slow} is the carrier mobility of the slower carrier, *e* is the elementary charge, *G* is the photogeneration rate and *V* is the applied bias voltage. In figure 4b the power at *V* for segment 3 is 0.46, which is approximately equal to 0.50, indicating space-charge photoconduction as possible correct physical description of the regime. The following different non-linear charge transport mechanisms in segments 4 and 5, is the fingerprint of SCLC conduction of wide-band gap semiconductor Schottky electrodes. In these electrodes, SCLC transport is triggered by a concentration of deep-level trapping states in the forbidden energy band gap, related to point defects and dislocations in the bulk material.[66] In segment 4, the photocurrent enters the trap-filled limit (TFL) SCLC regime. In this region, the voltage becomes sufficient to fill the majority of electrically active trap states in the material. This marks a transition from TFL regime to a regime where the density of free carriers begins to dominate.[67] The current rises steeply as the remaining traps are filled, resulting in a nonlinear increase characterized by a power-law dependence[67]:

$$I_{ph} \propto V^m, \tag{17}$$

with m > 2. Upon further increase in voltage, the *I*-*V* characteristic transitions into the trap-free SCLC regime. In this regime, all trap states are assumed to be filled, and the current is solely governed by the transport of free carriers under space-charge-limited conditions.[68] The *I*-*V* behavior follows the Mott-Gurney law, with the current scaling quadratically with voltage[69]:

$$I_{ph} = \frac{9}{8} \cdot \epsilon \cdot \mu \cdot \frac{V^2}{L^3}, \tag{18}$$

where ϵ is the dielectric constant, μ is the carrier mobility, *V* is the applied bias voltage and *L* is the effective transport layer thickness. The slope of segment 5, which is 1.96 $\approx$ 2, confirms the trap-free SCLC regime. There is an alternative theory that attributes segments 2 and 3 to charge carrier tunneling and segments 4 and 5 to the avalanche effect.[70]

The asymmetry in the *I*-*V* characteristics of figure 2 can be explained by small geometric differences in the electrodes in conjunction with surface states at the metal-semiconductor interfaces,

mostly acting as traps for holes. Consequently, one electrode being slightly bigger as the other, the density of trapped holes is relatively higher when a negative bias voltage is applied.[71,72] Hole traps in the bulk of the doped diamond can be doping impurities, vacancies, interstitials or complexes. In addition, when the photogeneration region is closer to one electrode, the barrier height of that Schottky junction decreases more than the other one, contributing to the asymmetry in the *I-V* characteristic.[66] The voltage offsets in the *I-V* characteristics of figure 2 represent turn-on voltages in the metal-semiconductor devices.[16]

The external quantum efficiency *EQE* was evaluated for the two-photon ionization process, adapted from Kumar et al.[73]:

$$EQE_{2P}(\%) = \frac{2 \cdot I_{ph} \cdot h \cdot c}{e \cdot P \cdot \lambda \cdot (1 - exp(-n_{NV} \cdot \sigma \cdot d))}, \tag{19}$$

where I_{ph} is the steady-state photocurrent, h is Planck's constant (6.626x10^{-34} m^{2}kgs^{-1}), c is the speed of light (3x10^8 ms^{-1}), e is the elementary charge, P is the incident optical power, λ is the illumination wavelength, n_{NV} is the density of NV$^-$ centers, σ is the respective peak stimulated emission cross-section and d is the thickness of the N-doped region. The factor of 2 accounts for the fact that two photons are required to liberate one electron via two-photon absorption. The effective density of NV$^-$ centers that contributes to the photocurrent can be calculated by:

$$n_{NV}^{eff} = \frac{PLcounts}{R_{emit} \cdot \eta_{coll} \cdot \pi \cdot r^2 \cdot d}, \tag{20}$$

where *PL counts* is a measure for emitted photons due to NV$^-$ relaxation per second, R_{emit} is the emission rate of photons per second per NV$^-$ center, η_{coll} is the photon collection efficiency, r is the radius of the laser spot and d is the thickness of the N-doped region. Equation (19) provides an estimate of the charge collection efficiency relative to the total photon flux incident on the device. A low EQE_{2P} may indicate limited ionization efficiency, suboptimal absorption, or poor carrier extraction. A second assessment of the charge collection at the electrodes for each photogenerated charge carrier is the photoelectric gain γ.[74] In terms of the two-photon ionization process of NV$^-$ centers, the photoelectric gain γ is equal to the ratio between the recombination lifetime of charge carriers τ and the electron transit time $t_{transit}$.[12] $t_{transit}$ is defined as:

$$t_{transit} = \frac{L^2}{\mu \cdot U}, \tag{21}$$

where L is the distance between electrodes, μ is the electron mobility and U is the applied bias voltage. This leads to the following expression for the photoelectric gain γ:

$$\gamma = \frac{\tau \cdot \mu \cdot U}{L^2}. \tag{22}$$

Figure 5a shows contact resistance measurements on the TLM line of sample B as deposited, after oxygen plasma treatment and after reactive ion etching (RIE) with an oxygen plasma, as a function of TLM pad spacing. The R^2 of the fits in figure 5a are so bad (< 0.3) that the following calculated values are considered questionable. This emphasizes the difficulty of understanding and fabricating low-resistance ohmic electrodes on the diamond sample. However, they are given because they are important values for evaluation of the manufactured electrodes and are popular in literature. The measurement points are from a single measurement and the error bars are the deviation from the fit. The specific contact resistance ρ_C following TLM[75], is:

$$R_C \approx \frac{\rho_C}{Z \cdot L_T} = \frac{\sqrt{R_s \cdot \rho_C}}{Z}; \tag{23}$$

$$\rho_C = \frac{(R_C \cdot Z)^2}{R_s}, \tag{24}$$

where R_C is the contact resistance, Z is the TLM pad width, L_T is the transfer length and R_s is the sheet resistance. The total resistance intercept in 5a equals two times the contact resistance R_C. The slope in 5a equals $\frac{R_s}{Z}$, with TLM pad width Z 564 μm. The specific contact resistance ρ_C as deposited is 3 Ωcm^2, after oxygen plasma treatment is 1 Ωcm^2 and after RIE with oxygen plasma is 2x10^6 Ωcm^2. A metal-semiconductor electrode is ohmic if it has a negligible contact resistance ρ_C relative to the bulk of the semiconductor material. Reported values for the specific contact resistance ρ_C of bulk N-doped diamond are around $10^{4\text{-}5}$ Ωcm^2[76], while that of oxygen terminated diamond is approximately 10^{20} Ωcm^2[77]. Dependent on which of these values is considered, the measured specific contact resistance ρ_C of 2x10^6 Ωcm^2, the fabricated contacts are ohmic or non-ohmic. Moreover, the measured values for specific contact resistance ρ_C, especially after etching, indicate high resistive electrodes and therefore do not correspond to low-resistance ohmic electrodes.[20,78] The transfer length L_T gives the main part of the area underneath a metallic electrode through which current enters the metal via the metal-

semiconductor interface:

$$L_T = \frac{\rho_C}{\sqrt{R_s \cdot \rho_C}}. \tag{25}$$

The transfer length L_T as deposited is 10 μm, after oxygen plasma treatment is 2 μm and after RIE with oxygen plasma is 0.28 μm. These calculated values are reasonable for the fabricated electrodes. The width of an electrode is 7.5 μm, so it is certain that all current is collected. Besides the fact that the TLM model does not fit the measured data well, the inconsistency of TLM pads fabrication also contributes to questioning these results.

Figure S8 of the supplementary materials for Siyushev et al.[14] indicates a photocurrent I_{ph} of approximately 1.6 pA for a laser ($\approx$ 532 nm) power P of 5 mW. The *PL counts* at 5 mW was 38x10^3 emitted photons per second, the thickness of the N-doped diamond layer was 15 μm and the illuminated area is considered a circle with diameter 1 μm.[14] The emission rate of photons per second per NV$^-$ center R_{emit} is approximately 2.5x10^6 s^{-1}[79], the photon collection efficiency η_{coll} was 0.16%[14] and the respective peak stimulated emission cross-section is approximately 3.6x10^{-21} m^2[80]. Following equation (19) and (20), the EQE_{2P} for the PDMR electrode configuration of Siyushev et al.[14] is 3%. The EQE_{2P} for the SCLC electrode configuration of sample B, corresponding to figure 5b is 500 $\pm$ 80%. The photocurrent I_{ph} was around 23.05 $\pm$ 4.15 pA, the corresponding *PL counts* was 4, 075 emitted photons per second and the laser power P was 5 mW. The other parameters were the same as those in the EQE_{2P} calculation for Siyushev et al. .[14] The EQE_{2P} of the fabricated electrodes shows an improvement over the electrode configuration of Siyushev et al. .[14] The distance between electrodes L is 5x10^{-4} cm and the applied bias voltage U is 22 V for the electrode configuration of Siyushev et al. when measuring PDMR.[14] An electron mobility μ of 3.6x10^2 cm^{2}V^{-1}s^{-1}[59] and a recombination lifetime τ between 80 ps and 3 ns[81] are assumed. These values are typical for the bulk material of N-doped type-Ib diamond, which corresponds to the diamond layer holding NV$^-$ centers of samples A and B as well as the sample of Siyushev et al.[14].[12] The electron mobility μ fluctuates depending on doping concentration[82], but the assumption made here is consistent with that of Bourgeois et al.[12]. Following equation (22), the photoelectric gain γ is estimated between 3 and 100 for the electrode configuration of Siyushev et al. .[14] Bourgeois et al. reported electrodes with a photoelectric gain γ between 1 and 40.[12] The photoelectric gain γ of the fabricated electrodes lies between 10 and 400, assuming the same electron mobility μ[59] and recombination lifetime τ[81].[14] If the calculated minority carrier recombination lifetime τ_n (2.6111 $\pm$ 0.6018 μs) of

the photoconductive electrode of sample B from equation (14) is considered correct, the photoelectric gain γ improves even more significantly to a value of 400, 000. The photoelectric gain γ improves in each case compared to the electrode configuration of Siyushev et al.[14] and Bourgeois et al.[12]. The difference in surface termination of the B-doped diamond layer between sample A and B may contribute to the difference in photocurrent response, but due to different N-doping concentrations and the inconsistent electrode fabrication process, no clear conclusions can be drawn in this work.

Figure 5b shows a simultaneous measurement of the intensity of photoluminescence and photocurrent while scanning the microwave frequency in the absence of an external magnetic field. Minima are observed at the resonant microwave frequency. The split in the dip at resonant frequency is due to magnetic noise in the bulk material of the sample. The PDMR signal shows good coherence with the optically detected magnetic resonance (ODMR) signal, but there is an additional unexplained dip at 2, 860 MHz, which does not contribute to the measurement of electron spin resonances of NV centers.

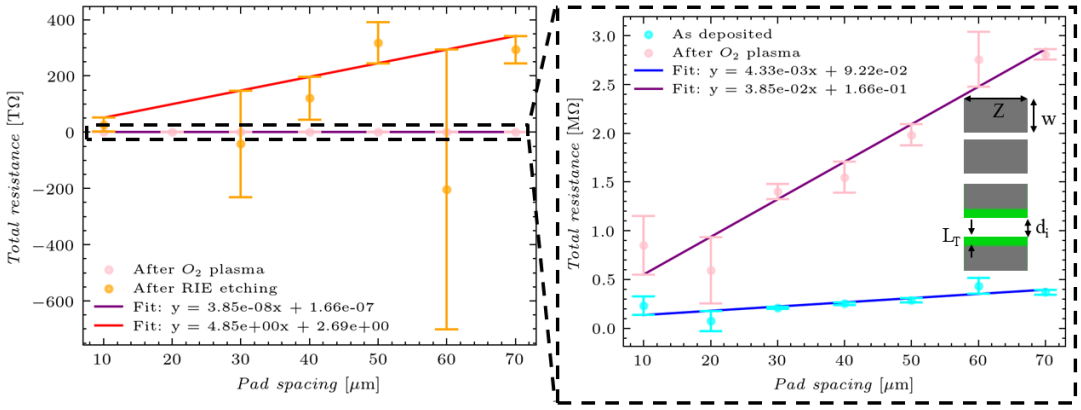

(a)

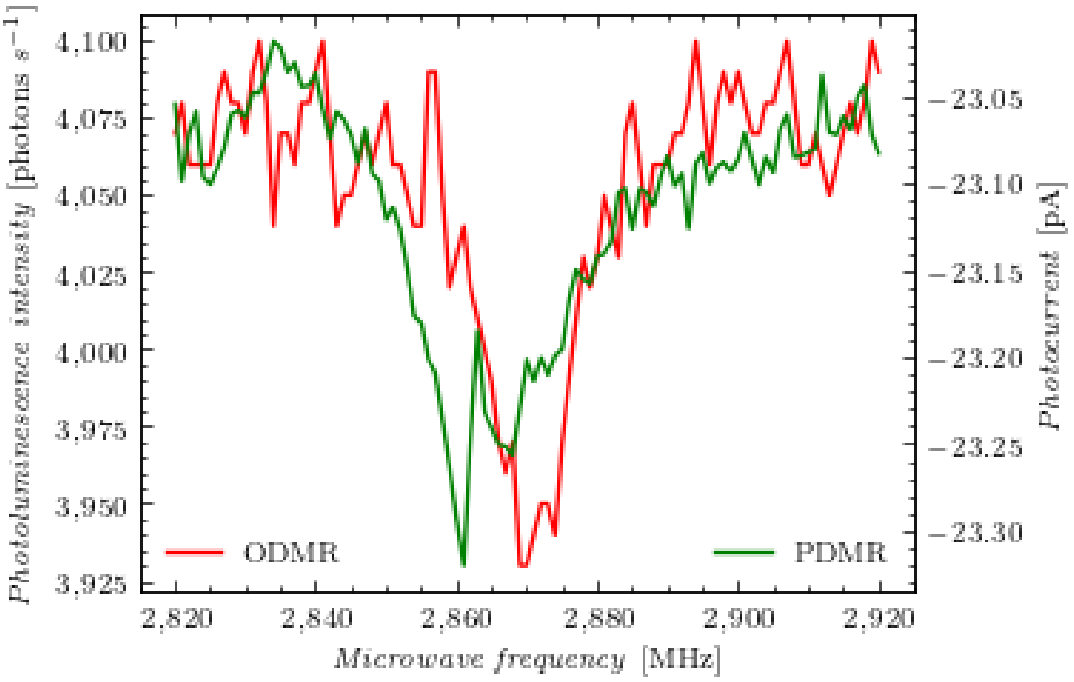

(b)

Figure 5. (a) The measured contact resistance ρ_C on the transfer length method (TLM) line of sample B as deposited, after oxygen plasma treatment and after reactive ion etching (RIE) with an oxygen plasma as a function of TLM pad spacing. (b) Comparison of ODMR and PDMR spectra recorded simultaneously. Sample B, green light power: 40 mW, applied electric field: 6.67x10^4 Vcm^{-1}, distance between electrodes: 15 μm.

3 Interdisciplinary Nature and Sustainability

In this research, both techniques and principles of materials chemistry and materials physics were included. The chemical manipulation of doping gasses and thermal conditions directly impacts the electrical behavior of the microwave plasma-enhanced chemical vapor deposition (MW PE CVD) grown N- and B-doped diamond layers.[7] The variation in current response between sample A and B demonstrated how surface chemistry (termination and treatment) critically influences charge transport and electrode performance. Analysis of the *I-V* characteristic, the specific contact resistance ρ_C and photoelectric gain γ involves models of charge carrier quantum tunneling, photoconductive behavior and SCLC, all central in solid-state semiconductor physics. The synergy between materials chemistry and materials physics is especially evident in the use of a B-doped layer (chemical process) to enable quantum tunneling (physical process). Thus, this work embodies a materiomicus approach: a systematic investigation of the properties of materials from atomic-level doping to device-scale transport, bridging chemistry and physics to optimize materials for quantum technologies. The use of diamond offers long device lifetimes and disables environmentally costly cryogenic cooling.[83] In addition to the environmental awareness on the footprint of quantum computing, there is a nascent research field on how to use quantum computing principles for specific climate-resilience challenges.[84]

4 Conclusion

In this work, the electrode configuration of PDMR was altered. Conventional PDMR implements back-to-back Schottky diodes configuration of Ti/Al on N-doped diamond, which limits photocurrent extraction due to high specific contact resistance ρ_C and inefficient carrier transport. To improve the current response, a thin B-doped diamond layer was incorporated in the electrode stack. The fabricated electrodes were evaluated with *I-V* characteristics, TLM, photoelectric gain γ and two-photon external quantum efficiency EQE_{2P}. The fabricated electrodes demonstrate significant improvements over the reference configuration reported by Siyushev et al.[14], particularly in approaching ohmic current response and photoelectric gain γ, improving from a value between 3 and 100 to a value between 10 and 400. The high specific contact resistance ρ_C, measured by TLM, of $2\text{x}10^6$ Ωcm^2 after RIE with oxygen plasma indicates a failure in the fabrication of low-resistance electrodes. Beyond empirical optimization, this study offers physical descriptions of the obtained *I-V* characteristics of back-to-back Schottky diodes

configuration going toward ohmic electrodes in series, of photoconductive responses of metal-semiconductor interfaces and of rarely described SCLC electrodes, starting in a photoconductor regime and transitioning to SCLC regime through trap-controlled and space-charge conduction with surface or interface recombination losses. These insights reinforce the critical role of interface control and diamond doping in the fabrication of low-resistance PDMR electrodes. This research contributes to the improvement of charge carrier transport in PDMR. In general, the integration of ohmic-like electrode structures into diamond platforms with color centers advances the potential for robust, high speed, room temperature, practical quantum technologies. Future research should focus on refining the fabrication consistency and exploring the role of surface termination, doping concentrations, annealing schemes and metallization schemes.

5 Experimental

Two samples were prepared with N- and B-doped diamond layers, which will be referred to as A and B for the remainder of the letter. A N-doped homoepitaxial layer was grown on a 3x3 mm^2 type Ib high-pressure high-temperature polished diamond substrate. A microwave plasma-enhanced chemical vapor deposition reactor (MW PE CVD) was utilized for the B-doped diamond layer with a base pressure of $3x10^{-7}$ mbar. The reactor was built by Mortet et al.[85], based on the reactor model developed at the Japanese National Institute of Research in Inorganic Materials[86]. N-doped diamond layers are grown in an ASTeX MW PE CVD reactor. For sample A, initial growth was performed at 4% CH_4 over 5 hours and using a 12, 000 ppm N_2:CH_4 ratio. The temperature was kept at roughly 950 °C as measured with a thermal camera (Optris PI 1m). After growth, the N-doped layer of sample A had a NV^- concentration of 182 ppb and a substitutional N concentration of 32 $\pm$ 5 ppm measured by double electron electron resonance spectroscopy. The N-doped layer of sample B was not characterized. A homoepitaxial B-doped diamond layer, approximately 300 nm thick, was grown on the N-doped diamond layer. The substrate temperature was maintained between 780 to 800 °C. A gaseous mixture of CH_4, trimethylborane and H_2 was used. The CVD plasma pressure was 250 mbar, the microwave power was 500 W, and the total gas flow was 500 sccm, with a constant [B]/[C] ratio of 997 ppm. Growth was carried out with a [CH_4]/[H_2] ratio of 1%, targeting a boron concentration of 10^{20} cm^{-3}. In sample B, the surface was oxidized with an acid cleaning procedure using boiling in 1:1 H_2SO_4/KNO_3 mixture before and after each growth step. In the acid cleaning procedure, 10 ml of H_2SO_4 is poured in a beaker and placed on a 350 °C hotplate with

a glass petri dish on top. When the H_2SO_4 is smoking, half of a laboratory sampling spoon of KNO_3 is added to the beaker, after which the sample is added to the mixture. After 15 minutes, a second half of a laboratory sampling spoon of KNO_3 is added to the beaker. At the end of the reaction, the beaker is removed from the hotplate and the glass petri dish is removed from the beaker. When the vaporization has stopped, the sample is ultrasonically cleaned for 5 minutes in deionized water. This ultrasonic cleaning step is repeated twice with fresh deionized water and isopropyl alcohol. The acid cleaning procedure ends with blowing the sample dry. In sample A, the final acid cleaning step was omitted, leaving it hydrogen-terminated from the last growth step. After each acid cleaning—or, in the case of sample A, after the last growth step—the sample underwent ultrasonic cleaning in acetone for 10 minutes, followed by ultrasonic cleaning in isopropyl alcohol for 10 minutes, and finally dried with nitrogen gas. **Figure 6** shows a schematic diagram of the process flow towards electrode fabrication, where each step is numbered and discussed in the following text. To determine specific contact resistance ρ_c of the electrodes, rectangular TLM patterns using rectangular patches of 564x200 μm^2 and gap spacings (d) of 10 to 70 µm in 10 µm increments were prepared on sample B (1) using direct-write photolithography (MicroWriter ML3 Baby, Durham Magneto Optics), coating the sample with a thin layer of photoresist (AZ 5214-E from MicroChemicals GmbH) (2), and wet chemical development (3). PDMR patterns are prepared simultaneously on samples A and B. Ti/Al (20/100 nm) bilayer metallization was performed using RF sputtering (Pfeiffer SPIDER 600) (4). After lift-off (5), the samples were exposed to a mild oxygen plasma of 50 W and 35 sccm O_2 (6). Next, the electrodes and TLM structures were vertically etched beyond the B-doped layer with a reactive ion etching (RIE) homemade plasma system using oxygen plasma of 300 W, 75 sccm Ar, 25 sccm O_2, at a base pressure of $3x10^{-6}$ and a working pressure of $2x10^{-2}$ mbar (7). Electrode fabrication was inconsistent with electrode pairs showing no photocurrent response and electrode pairs having non-zero dark current. *I-V* characteristics were measured with two setups in air at room temperature. **Figure 7a** illustrates setup 1 for *I-V* characteristic measurements. This system applies a bias voltage (model DC205 from Stanford Research Systems) across two coplanar electrodes and measures the dark current. The dark current is defined as the current measured between the two electrodes when a bias voltage is applied but no light, whether it is from a laser or from the environment, is hitting the sample. The dark current is therefore measured in a dark room (only setup light and black painted walls). The dark current was zero for all electrode configurations discussed in this work. The current is amplified by

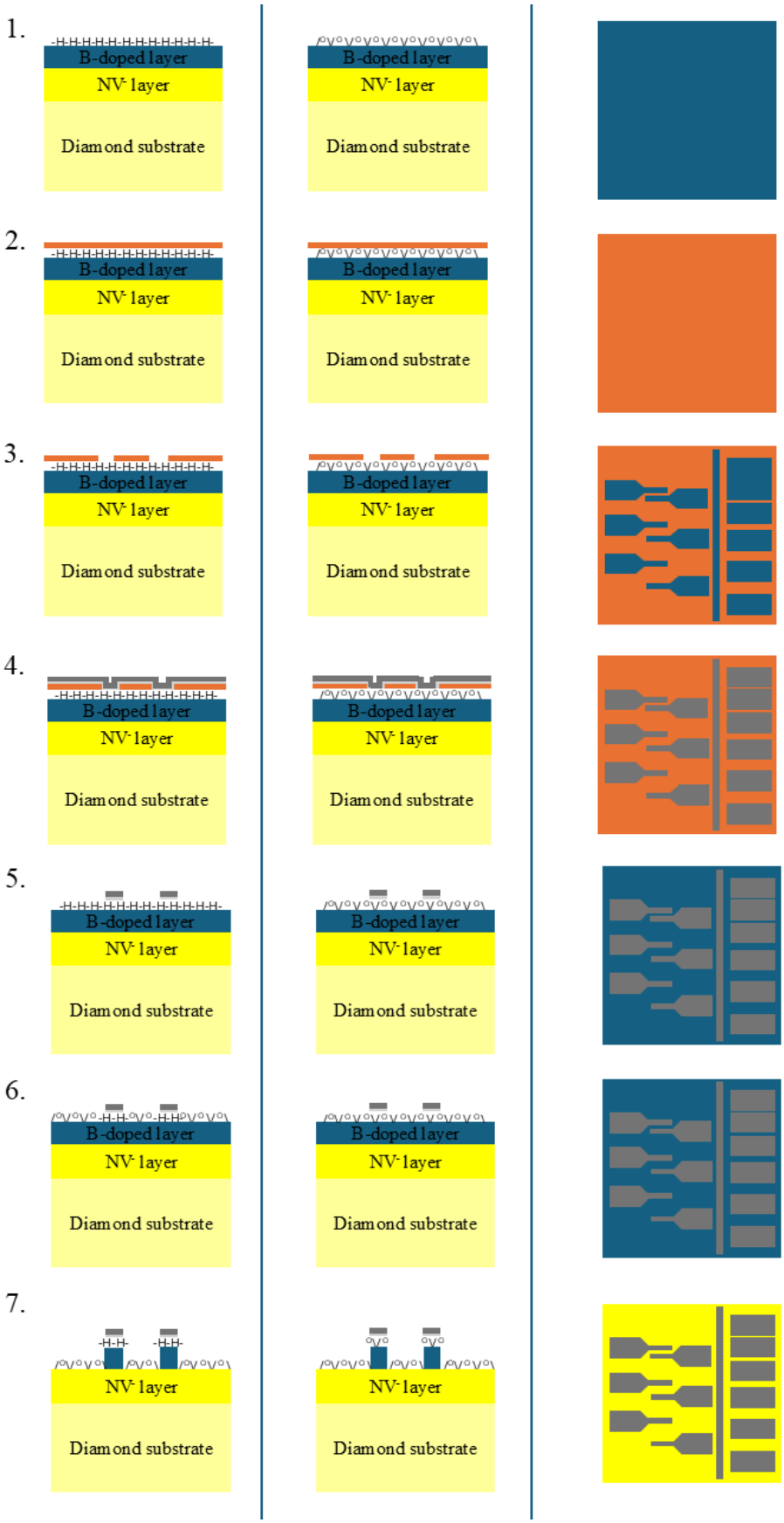

Figure 6. Schematic diagram of process flow towards electrode configuration and transfer length method (TLM) structure fabrication. The first column is for sample A, the second column for sample B and the third column for a representation of the top view of the samples with an impression of the electrode configuration and TLM structure design.

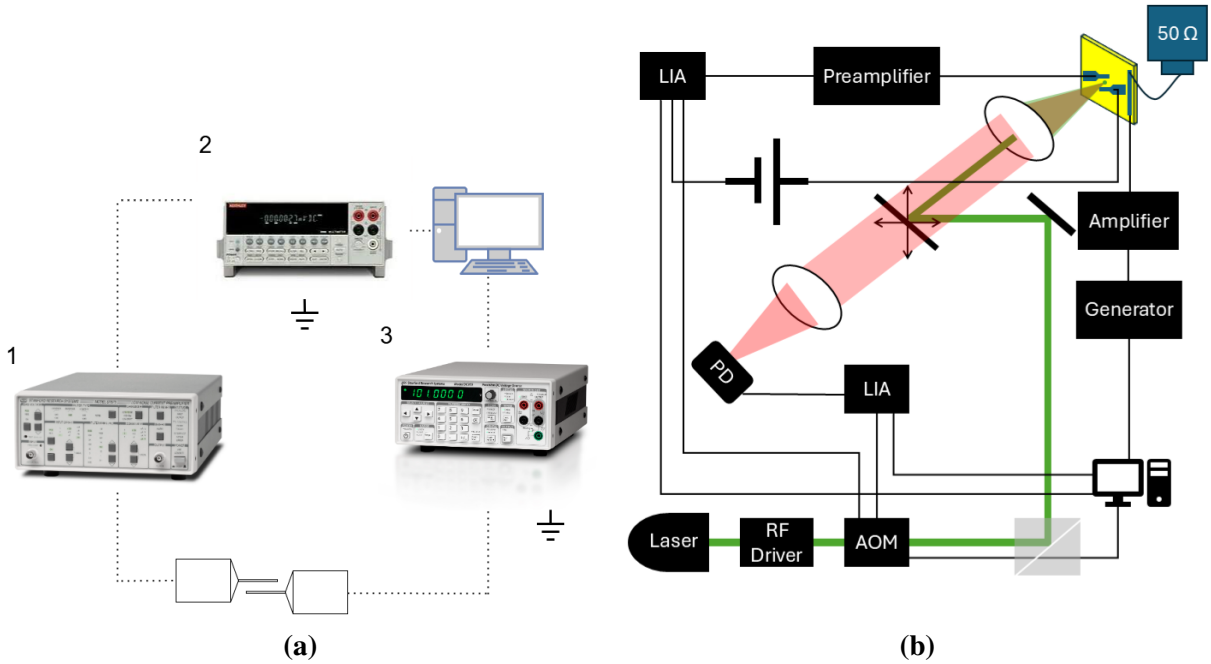

Figure 7. (a) Setup 1 for measuring *I*-*V* characteristics of dark current, which consists of (1) a low-noise current to voltage preamplifier (model SR570 from Stanford Research Systems), (2) a multimeter (model 2000 from Keithley) and (3) a DC voltage source (model DC205 from Stanford Research Systems). (b) Setup 2 for measuring *I*-*V* characteristics under laser light, which consists of laser Cobolt 06-DPL 561 nm and 100 W, an acousto-optical RF driver (model 1200AF-DIFO-1.0 from Gooch&Housego), an acousto-optical modulator (model 3200-146 from Crystal Technology), a kinematic fluorescence filter cube (model DFM1L/M from Thorlabs), a lock-in amplifier (model 7260 DSP from EG&G), a DC voltage source (model DC205 from Stanford Research Systems), a low-noise current to voltage preamplifier (model SR570 from Stanford Research Systems), a lock-in amplifier (model SR830 from Stanford Research Systems), a 50 Ω terminator, a MW generator (model OPX+ from QuantumMachines) and a broadband amplifier (model ZHL-16W-43+ from Mini-circuits). Setup 2 is also capable of measuring optically detected magnetic resonance (ODMR) spectra.

a low-noise current to voltage preamplifier (model SR570 from Stanford Research Systems) and measured using a multimeter (model 2000 from Keithley). **Figure 7b** shows setup 2 for *I-V* characteristic measurements under green laser light illumination. Setup 2 can also measure dark current by blocking the laser. Both dark measurements as with laser light are conducted in a dark room. The green laser light (532 nm) illumination is produced by a linearly polarized single-mode laser (model 06-DPL 561 nm and 100 W from Cobolt). The light is pulsed by an acousto-optical RF driver (model 1200AF-DIFO-1.0 from Gooch&Housego) and acousto-optical modulator (AOM) (model 3200-146 from Crystal Technology). The pulsed light beam is focused onto the diamond surface with an objective. Photoluminescence light (637-800 nm) resulting from the radiatively decay of the NV^- center's ^3E excited state to the $^3A_2$ ground state (figure 1b), is collected by the same objective and filtered with a kinematic fluorescence filter cube (model DFM1L/M from Thorlabs). The collected photoluminescence light is focused onto a photodiode (PD). Photogenerated electrons are driven towards the electrodes by applying a DC voltage (model DC205 from Stanford Research Systems) between the two coplanar electrodes. The photocurrent is amplified by a low-noise current to voltage preamplifier (model SR570 from Stanford Research Systems) and measured using a lock-in amplifier (LIA) (model SR830 from Stanford Research Systems) referenced to the AOM. Microwaves of controlled frequency are generated with a RF signal generator (model OPX+ from QuantumMachines). The MW power is set using a broadband amplifier (model ZHL-16W-43+ from Mini-circuits). The MW field is applied by a lithographically fabricated Ti/Al metal strip across the diamond surface and connected to a 50 Ω terminator. For extensive details on setup 2, please refer to 'Experimental setup.' under the 'Methods' section of Bourgeois et al. .[12] The *I-V* characteristics under laser illumination were measured in an area of 36 μm along the length of the electrode, with a characteristic measured every 4 μm at the location between the two electrodes with the highest positive current response.

Acknowledgements

First of all, I would like to thank Prof. Nesladek for hosting this master thesis and accepting me as a master student in his research group. I greatly appreciate the trust and freedom I was given in his labs. His scientific insight into my research results has prompted me to explore different hypotheses and gain insights that I previously did not consider possible.

Secondly, I would like to thank my daily supervisors dr. Kunnen and ing. Vandebosch. Dr. Kunnen specifically for teaching me experimental techniques such as lithography, metal deposition, lift-off, acid cleaning and etching. Ing. Vandebosch specifically for teaching me how to measure dark *I*-*V* characteristics and putting wire bonds. In addition, both of them, for their endless patience with me in explaining physical principles, explaining the meaning of my results, answering my questions, going through literature with me and revising this manuscript.

Thirdly, I would like to explicitly thank dr. Bourgeois for the many photocurrent measurements she performed for my fabricated electrodes. Furthermore, she always provided insightful explanations behind the obtained data, which formed a strong foundation for many explanations in this thesis. If this was not enough, she also trained me, next to dr. Petrov, to measure with the second setup, which laid the foundation for all *I*-*V* characteristics and the ODMR-PDMR measurement of this thesis.

Finally, I would like to thank the entire Q-lab research group of Prof. Nesladek and the people of IMO-IMOMEC for their warm welcome and constant readiness to help me. Specifically linked to this thesis, dr. Prooth for growing the diamond layers for this research, Mrs. Ahmed for explaining the sputtering tools at IMO, dr. Petrov for explaining various measurements, including PDMR, Prof. Hruby for the cleanroom retraining and general help and Mrs. Carmans for her insightful comments. Mr. Baccus for solving all technical problems for me, always showing me the correct way to act when I did something wrong and always being there for my questions and material needs. Mr. Cornille, Gijbels and Beerden for the non-scientific talks and fun times during work, and the last mentioned gentleman for the invitation to the campus run, what a run that was.

References

[1] Bas Hensen et al. “Loophole-free Bell inequality violation using electron spins separated by 1.3 kilometres”. In: *Nature* 526.7575 (2015), pp. 682–686.

[2] Nir Bar-Gill et al. “Solid-state electronic spin coherence time approaching one second”. In: *Nature communications* 4.1 (2013), p. 1743.

[3] Victor M Acosta et al. “Diamonds with a high density of nitrogen-vacancy centers for magnetometry applications”. In: *Physical Review B—Condensed Matter and Materials Physics* 80.11 (2009), p. 115202.

[4] David Le Sage et al. “Optical magnetic imaging of living cells”. In: *Nature* 496.7446 (2013), pp. 486–489.

[5] Jacob M Taylor et al. “High-sensitivity diamond magnetometer with nanoscale resolution”. In: *Nature Physics* 4.10 (2008), pp. 810–816.

[6] Thomas Wolf et al. “Subpicotesla diamond magnetometry”. In: *Physical Review X* 5.4 (2015), p. 041001.

[7] Lila VH Rodgers et al. “Materials challenges for quantum technologies based on color centers in diamond”. In: *MRS Bulletin* 46.7 (2021), pp. 623–633.

[8] Wen Yang, Wen-Long Ma, and Ren-Bao Liu. “Quantum many-body theory for electron spin decoherence in nanoscale nuclear spin baths”. In: *Reports on Progress in Physics* 80.1 (2016), p. 016001.

[9] Ashok Ajoy and Paola Cappellaro. “Perfect quantum transport in arbitrary spin networks”. In: *Physical Review B—Condensed Matter and Materials Physics* 87.6 (2013), p. 064303.

[10] David A Hopper, Henry J Shulevitz, and Lee C Bassett. “Spin readout techniques of the nitrogen-vacancy center in diamond”. In: *Micromachines* 9.9 (2018), p. 437.

[11] S Ali Momenzadeh et al. “Nanoengineered diamond waveguide as a robust bright platform for nanomagnetometry using shallow nitrogen vacancy centers”. In: *Nano letters* 15.1 (2015), pp. 165–169.

[12] Emilie Bourgeois et al. “Photoelectric detection of electron spin resonance of nitrogen-vacancy centres in diamond”. In: *Nature Communications* 6.1 (2015), p. 8577.

[13] Emilie Bourgeois, Michal Gulka, and Milos Nesladek. “Photoelectric detection and quantum readout of nitrogen-vacancy center spin states in diamond”. In: *Advanced Optical Materials* 8.12 (2020), p. 1902132.

[14] Petr Siyushev et al. “Photoelectrical imaging and coherent spin-state readout of single nitrogen-vacancy centers in diamond”. In: *Science* 363.6428 (2019), pp. 728–731.

[15] Jozef Osvald. “Back-to-back connected asymmetric Schottky diodes with series resistance as a single diode”. In: *physica status solidi (a)* 212.12 (2015), pp. 2754–2758.

[16] Simon M Sze, Yiming Li, and Kwok K Ng. *Physics of semiconductor devices*. John wiley & sons, 2021.

[17] Sheng S Li. “Metal–semiconductor contacts”. In: *Semiconductor Physical Electronics*. Springer, 2006, pp. 284–333.

[18] KL Moazed, JR Zeidler, and MJ Taylor. “A thermally activated solid state reaction process for fabricating ohmic contacts to semiconducting diamond”. In: *Journal of applied physics* 68.5 (1990), pp. 2246–2254.

[19] CA Hewett et al. “Specific contact resistance measurements of ohmic contacts to semiconducting diamond”. In: *Journal of Applied Physics* 77.2 (1995), pp. 755–760.

[20] Yinyue Wang et al. “Ohmic contacts and interface properties of Au/Ti/p-diamond prepared by rf sputtering”. In: *Surface and Interface Analysis: An International Journal devoted to the development and application of techniques for the analysis of surfaces, interfaces and thin films* 29.7 (2000), pp. 478–481.

[21] T Tachibana, BE Williams, and JT Glass. “Correlation of the electrical properties of metal contacts on diamond films with the chemical nature of the metal-diamond interface. I. Gold contacts: A non-carbide-forming metal”. In: *Physical Review B* 45.20 (1992), p. 11968.

[22] K Nishimura, K Das, and JT Glass. “Material and electrical characterization of polycrystalline boron-doped diamond films grown by microwave plasma chemical vapor deposition”. In: *Journal of applied physics* 69.5 (1991), pp. 3142–3148.

[23] V Venkatesan et al. “Evaluation of ohmic contacts formed by B+ implantation and Ti-Au metallization on diamond”. In: *Journal of applied physics* 74.2 (1993), pp. 1179–1187.

[24] Goro Kawaguchi et al. “Dependence of contact resistance on metal electronegativity for B-doped diamond films”. In: *Journal of applied physics* 75.10 (1994), pp. 5165–5170.

[25] KL Moazed, Richard Nguyen, and James R Zeidler. “Ohmic contacts to semiconducting diamond”. In: *IEEE electron device letters* 9.7 (1988), pp. 350–351.

[26] C Johnston et al. “High temperature contacts to chemically vapour deposited diamond films—reliability issues”. In: *Materials Science and Engineering: B* 29.1-3 (1995), pp. 206–210.

[27] M Roser et al. “High temperature reliability of refractory metal ohmic contacts to diamond”. In: *Journal of the Electrochemical Society* 139.7 (1992), p. 2001.

[28] Johan F Prins. “Preparation of ohmic contacts to semiconducting diamond”. In: *Journal of Physics D: Applied Physics* 22.10 (1989), p. 1562.

[29] Jiro Nakanishi et al. “Formation of ohmic contacts to p-type diamond using carbide forming metals”. In: *Journal of Applied Physics* 76.4 (1994), pp. 2293–2298.

[30] Matthias Werner. “Diamond metallization for device applications”. In: *Semiconductor science and technology* 18.3 (2003), S41.

[31] F Maier et al. “Origin of surface conductivity in diamond”. In: *Physical review letters* 85.16 (2000), p. 3472.

[32] T Teraji, S Koizumi, and Y Koide. “Ohmic contact for p-type diamond without postannealing”. In: *Journal of Applied Physics* 104.1 (2008), p. 016104.

[33] Shenda M Baker, George R Rossman, and John D Baldeschwieler. “Observation of surface charge screening and Fermi level pinning on a synthetic, boron-doped diamond”. In: *Journal of applied physics* 74.6 (1993), pp. 4015–4019.

[34] T Teraji et al. “Low-leakage p-type diamond Schottky diodes prepared using vacuum ultraviolet light/ozone treatment”. In: *Journal of Applied Physics* 105.12 (2009), pp. 126109–126109–3.

[35] Yoshikatsu Jingu, Kazuyuki Hirama, and Hiroshi Kawarada. “Ultrashallow TiC source/drain contacts in diamond MOSFETs formed by hydrogenation-last approach”. In: *IEEE transactions on electron devices* 57.5 (2010), pp. 966–972.

[36] Jung-Hun Seo et al. “Thermal diffusion boron doping of single-crystal natural diamond”. In: *Journal of Applied Physics* 119.20 (2016), pp. 205703–1–205703–8.

[37] Holly M Johnson et al. “Cleaning diamond surfaces via oxygen plasma inhibits the formation of a TiC interface”. In: *Diamond and Related Materials* 126 (2022), p. 109058.

[38] Engin Arslan et al. “Tunneling current via dislocations in Schottky diodes on AlInN/AlN/GaN heterostructures”. In: *Semiconductor science and technology* 24.7 (2009), p. 075003.

[39] Mei Wu et al. “Schottky forward current transport mechanisms in AlGaN/GaN HEMTs over a wide temperature range”. In: *Chinese Physics B* 23.9 (2014), p. 097307.

[40] Simone Milazzo et al. “Tunneling and thermionic emission as charge transport mechanisms in W-based Schottky contacts on AlGaN/GaN heterostructures”. In: *Applied Surface Science* 679 (2025), p. 161316.

[41] DY Liu et al. “Nitrogen modulation of boron doping behavior for accessible n-type diamond”. In: *APL materials* 9.8 (2021), pp. 081106–1–081106–9.

[42] D Donoval et al. “Current transport and barrier height evaluation in Ni/InAlN/GaN Schottky diodes”. In: *Applied Physics Letters* 96.22 (2010), pp. 223501–1–223501–3.

[43] Engin Arslan et al. “Dislocation-governed current-transport mechanism in (Ni/Au)–AlGaN/AlN/GaN heterostructures”. In: *Journal of Applied Physics* 105.2 (2009), pp. 023705–1–023705–7.

[44] Makoto Kawano et al. “Ferromagnetic permalloy/p-type boron-doped diamond Schottky barrier diodes”. In: *Applied Physics Letters* 126.1 (2025), pp. 012107–1–012107–5.

[45] Yoshiaki Mokuno et al. “A nitrogen doped low-dislocation density free-standing single crystal diamond plate fabricated by a lift-off process”. In: *Applied Physics Letters* 104.25 (2014), pp. 252109–1–252109–4.

[46] Christoph E Nebel. “Nitrogen-vacancy doped CVD diamond for quantum applications: A review”. In: *Semiconductors and Semimetals* 103 (2020), pp. 73–136.

[47] Jaehyeok Park et al. “Extracting the inherent ideality factor of a diode from electrical current–voltage characteristics”. In: *Electronics Letters* 59.23 (2023), e13046.

[48] CP Harisha et al. “Negative Schottky barrier height and surface inhomogeneity in n-silicon M–I–S structures”. In: *AIP Advances* 12.7 (2022), pp. 075117–1–075117–8.

[49] Xumei Zhao et al. “Tuning the Schottky barrier height in single-and bi-layer graphene-inserted MoS2/metal contacts”. In: *Scientific Reports* 14.1 (2024), p. 20905.

[50] Hitoshi Umezawa et al. “Characterization of leakage current on diamond Schottky barrier diodes using thermionic-field emission modeling”. In: *Diamond and related materials* 15.11-12 (2006), pp. 1949–1953.

[51] Hitoshi Umezawa et al. “Leakage current analysis of diamond Schottky barrier diode”. In: *Applied physics letters* 90.7 (2007), pp. 073506–1–073506–3.

[52] Hitoshi Umezawa et al. “Leakage current analysis of diamond Schottky barrier diodes by defect imaging”. In: *Diamond and related materials* 40 (2013), pp. 56–59.

[53] V Mikhelashvili, R Padmanabhan, and G Eisenstein. “Simplified parameter extraction method for single and back-to-back Schottky diodes fabricated on silicon-on-insulator substrates”. In: *Journal of Applied Physics* 122.3 (2017), pp. 034503–1–034503–9.

[54] Lingzhi Luo et al. “MXene-GaN van der Waals metal-semiconductor junctions for high performance multiple quantum well photodetectors”. In: *Light: Science & Applications* 10.1 (2021), p. 177.

[55] Huimin Zhu et al. “Progress and applications of (Cu–) Ag–Bi–I semiconductors, and their derivatives, as next-generation lead-free materials for photovoltaics, detectors and memristors”. In: *International Materials Reviews* 69.1 (2024), pp. 19–62.

[56] Yingjie Zhang et al. “Ultrasensitive photodetectors exploiting electrostatic trapping and percolation transport”. In: *Nature Communications* 7.1 (2016), p. 11924.

[57] T Murooka et al. “Photoelectrical detection of nitrogen-vacancy centers by utilizing diamond lateral p–i–n diodes”. In: *Applied Physics Letters* 118.25 (2021), pp. 253502–1–253502–7.

[58] Yaping Dan et al. “A photoconductor intrinsically has no gain”. In: *Acs Photonics* 5.10 (2018), pp. 4111–4116.

[59] T Malinauskas et al. “Optical evaluation of carrier lifetime and diffusion length in synthetic diamonds”. In: *Diamond and Related Materials* 17.7-10 (2008), pp. 1212–1215.

[60] RJ Fleming. “Trap-controlled transient photoconductivity in dielectrics”. In: *Journal of Applied Physics* 50.12 (1979), pp. 8075–8081.

[61] W Tomaszewicz and B Jachym. “Dispersive carrier transport in solids with continuous trap distribution”. In: *Journal of non-crystalline solids* 65.2-3 (1984), pp. 193–213.

[62] IK Kristensen and JM Hvam. “Dispersive transport and trap saturation in doped hydrogenated amorphous silicon”. In: *Solid state communications* 50.9 (1984), pp. 845–848.

[63] George FA Dibb et al. “Analysis of the relationship between linearity of corrected photocurrent and the order of recombination in organic solar cells”. In: *The Journal of Physical Chemistry Letters* 2.19 (2011), pp. 2407–2411.

[64] VD Mihailetchi, J Wildeman, and Paul WM Blom. “Space-charge limited photocurrent”. In: *Physical review letters* 94.12 (2005), p. 126602.

[65] Z-E Ooi et al. “Analysis of photocurrents in lateral-geometry organic bulk heterojunction devices”. In: *Applied Physics Letters* 101.5 (2012), pp. 053301–1–053301–5.

[66] Marco Girolami et al. “Self-powered solar-blind ultrafast UV-C diamond detectors with asymmetric Schottky contacts”. In: *Carbon* 189 (2022), pp. 27–36.

[67] Murray A Lampert. “Simplified theory of space-charge-limited currents in an insulator with traps”. In: *Physical Review* 103.6 (1956), p. 1648.

[68] A Rose. “Space-charge-limited currents in solids”. In: *Physical Review* 97.6 (1955), p. 1538.

[69] NF Mott and RW Gurney. *Electronic Processes in Ionic Crystals Oxford*. 1940.

[70] Zhangcheng Liu et al. “Responsivity improvement of Ti–diamond–Ti structured UV photodetector through photocurrent gain”. In: *Optics express* 26.13 (2018), pp. 17092–17098.

[71] Linpeng Dong et al. “Self-powered MSM deep-ultraviolet β-Ga2O3 photodetector realized by an asymmetrical pair of Schottky contacts”. In: *Optical Materials Express* 9.3 (2019), pp. 1191–1199.

[72] Wei Gao et al. “2D WS2 based asymmetric Schottky photodetector with high performance”. In: *Advanced Electronic Materials* 7.7 (2021), p. 2000964.

[73] Krishan Kumar and Davinder Kaur. “A review on recent advancements in the growth of MoS2 based flexible photodetectors”. In: *Solar Energy Materials and Solar Cells* 268 (2024), p. 112736.

[74] Richard H Bube and Stuart A Rice. *Photoconductivity of solids*. 1961.

[75] HH Berger. “Solid State Electron.” In: *Solid-State Electron* 15.145 (1972), pp. 90048–2.

[76] Yuki Matsushima et al. “Fabrication and characterization of diamond (100) p+-i-n+ diodes with heavily nitrogen-doped films”. In: *Diamond and Related Materials* 145 (2024), p. 111116.

[77] Atsushi Otake et al. “Sluggish Electron Transfer of Oxygen-Terminated Moderately Boron-Doped Diamond Electrode Induced by Large Interfacial Capacitance between a Diamond and Silicon Interface”. In: *JACS Au* 4.3 (2024), pp. 1184–1193.

[78] Congmian Zhen et al. “Characteristics of Au/Ti/p-diamond ohmic contacts prepared by rf sputtering”. In: *Surface and Interface Analysis: An International Journal devoted to the development and application of techniques for the analysis of surfaces, interfaces and thin films* 32.1 (2001), pp. 106–109.

[79] Felix A Hahl et al. “Magnetic-field-dependent stimulated emission from nitrogen-vacancy centers in diamond”. In: *Science advances* 8.22 (2022), eabn7192.

[80] Elisabeth Fraczek et al. “Laser spectroscopy of NV-and NV0 colour centres in synthetic diamond”. In: *Optical Materials Express* 7.7 (2017), pp. 2571–2585.

[81] Patrik Ščajev et al. “Nonequilibrium carrier dynamics in bulk HPHT diamond at two-photon carrier generation”. In: *physica status solidi (a)* 208.9 (2011), pp. 2067–2072.

[82] Nazareno Donato et al. “Diamond power devices: state of the art, modelling, figures of merit and future perspective”. In: *Journal of Physics D: Applied Physics* 53.9 (2019), p. 093001.

[83] Nivedita Arora and Prem Kumar. “Sustainable quantum computing: Opportunities and challenges of benchmarking carbon in the quantum computing lifecycle”. In: *arXiv preprint arXiv:2408.05679* (2024).

[84] Kin Tung Michael Ho et al. “Quantum computing for climate resilience and sustainability challenges”. In: *2024 IEEE International Conference on Quantum Computing and Engineering (QCE)*. Vol. 2. IEEE. 2024, pp. 262–267.

[85] Vincent Mortet et al. “Characterization of boron doped diamond epilayers grown in a NIRIM type reactor”. In: *Diamond and Related Materials* 17.7-10 (2008), pp. 1330–1334.

[86] Mutsukazu Kamo et al. “Diamond synthesis from gas phase in microwave plasma”. In: *Journal of crystal growth* 62.3 (1983), pp. 642–644.

Supporting

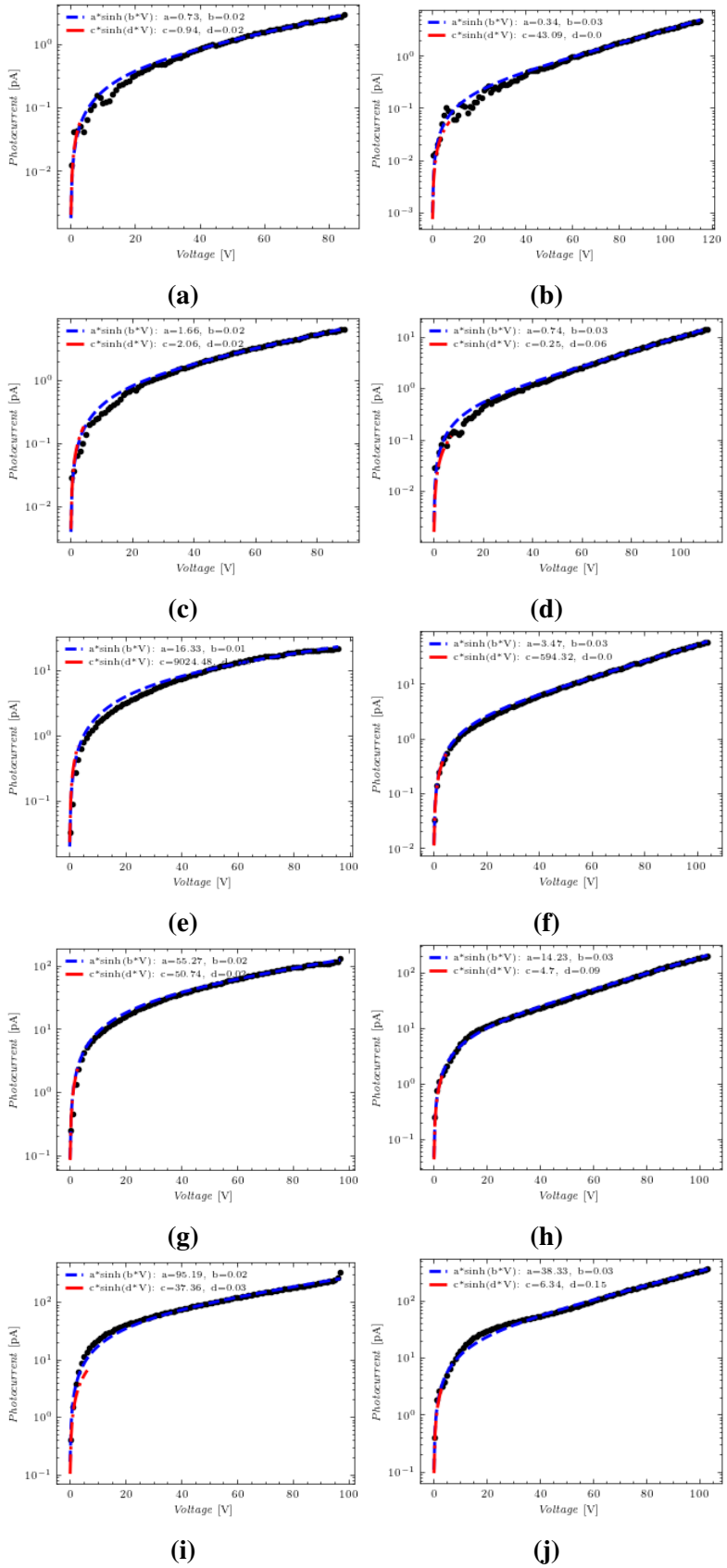

Figure S1. Similar to figure 3 for a) negative voltage sweep at 5 mW, b) positive voltage sweep at 5 mW, c) negative voltage sweep at 10 mW, d) positive voltage sweep at 10 mW, e) negative voltage sweep at 20 mW, f) positive voltage sweep at 20 mW, g) negative voltage sweep at 30 mW, h) positive voltage sweep at 30 mW, i) negative voltage sweep at 40 mW and j) positive voltage sweep at 40 mW (Sample A, electrode spacing of 5 μm).

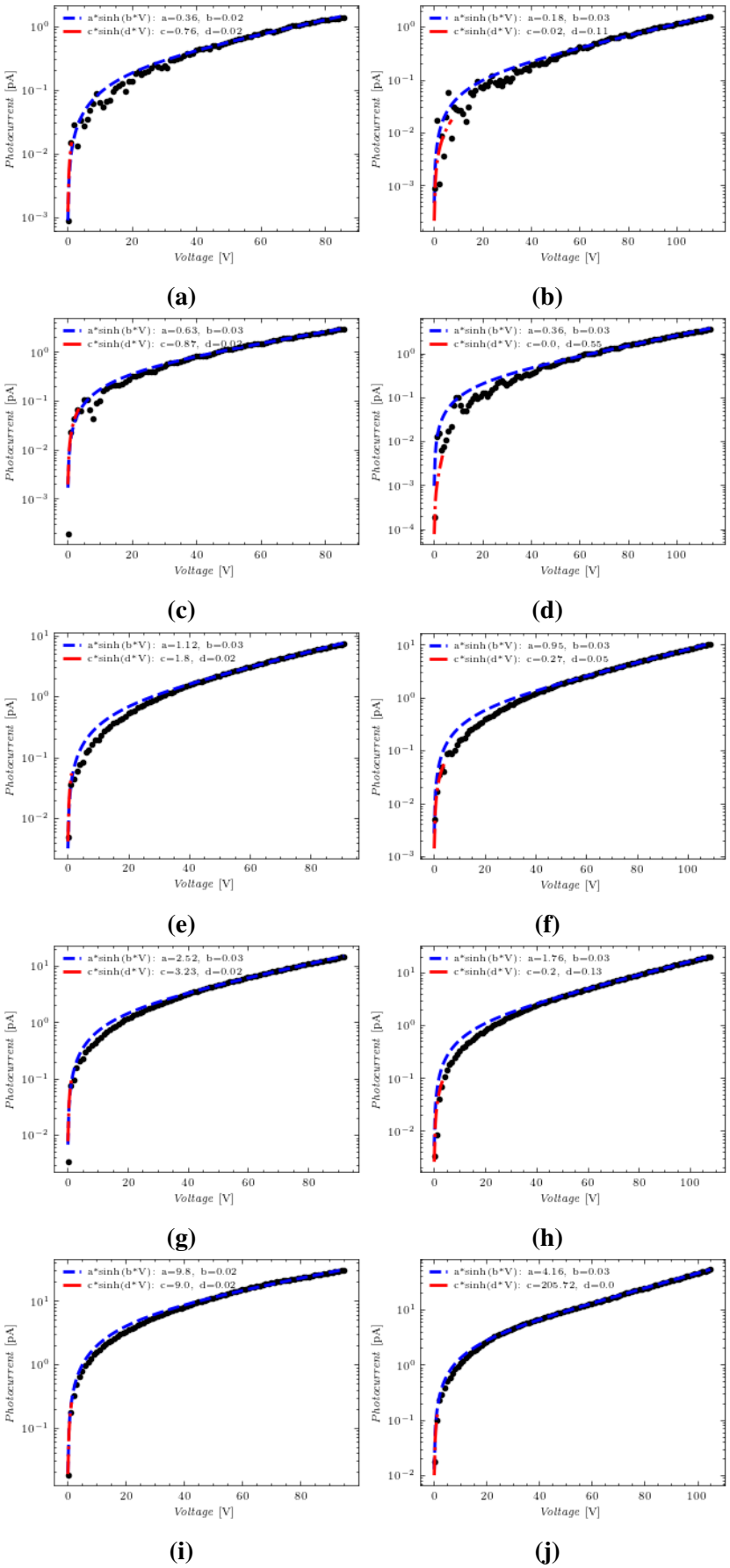

Figure S2. Similar to figure 3 for a) negative voltage sweep at 5 mW, b) positive voltage sweep at 5 mW, c) negative voltage sweep at 10 mW, d) positive voltage sweep at 10 mW, e) negative voltage sweep at 20 mW, f) positive voltage sweep at 20 mW, g) negative voltage sweep at 30 mW, h) positive voltage sweep at 30 mW, i) negative voltage sweep at 40 mW and j) positive voltage sweep at 40 mW (Sample A, electrode spacing of 7.5 μm).

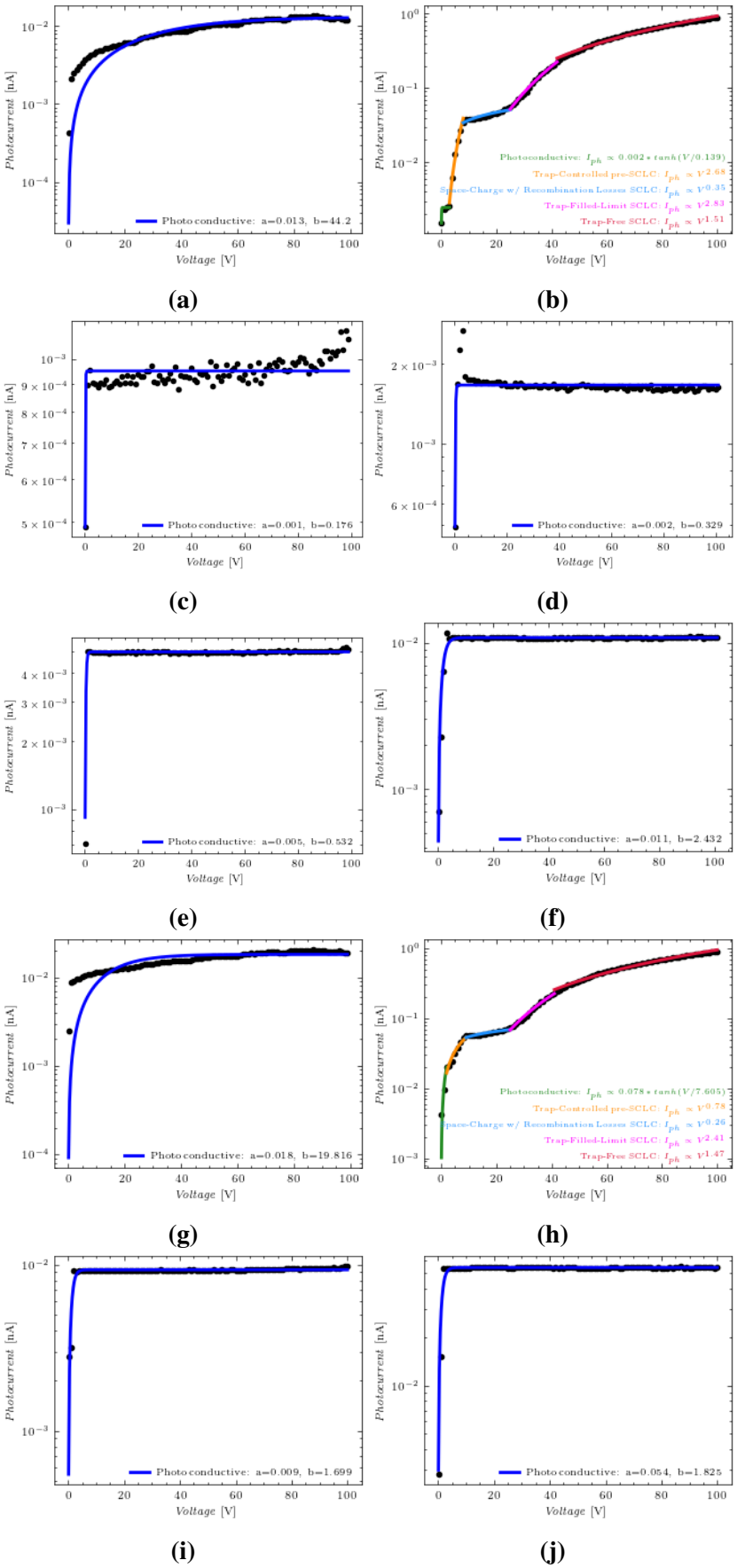

Figure S3. Similar to figure 4a and 4b for a) negative voltage sweep at 5 mW, b) positive voltage sweep at 5 mW, c) negative voltage sweep at 10 mW, d) positive voltage sweep at 10 mW, e) negative voltage sweep at 20 mW, f) positive voltage sweep at 20 mW, g) negative voltage sweep at 30 mW, h) positive voltage sweep at 30 mW, i) negative voltage sweep at 40 mW and j) positive voltage sweep at 40 mW (Sample B, electrode spacing of 5 μm).

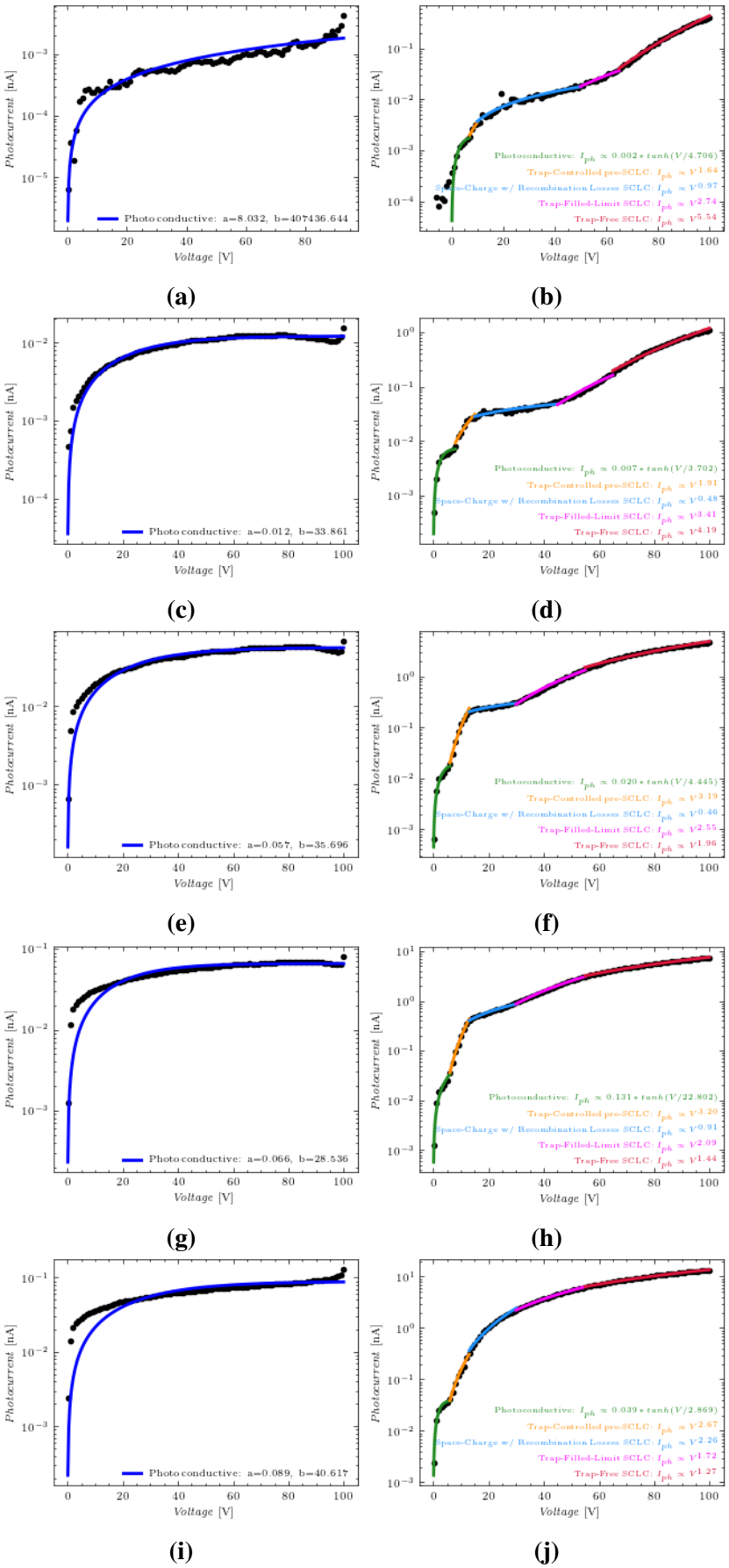

Figure S4. Similar to figure 4a and 4b for a) negative voltage sweep at 5 mW, b) positive voltage sweep at 5 mW, c) negative voltage sweep at 10 mW, d) positive voltage sweep at 10 mW, e) negative voltage sweep at 20 mW, f) positive voltage sweep at 20 mW, g) negative voltage sweep at 30 mW, h) positive voltage sweep at 30 mW, i) negative voltage sweep at 40 mW and j) positive voltage sweep at 40 mW (Sample B, electrode spacing of 15 μm).

Table S1. Ideality factor n values, calculated according equation (9), for all negative and positive voltage sweeps at every optical power of every measured electrode pair of sample A. The first character before the first underscore indicates the sample, the second character between the underscores indicates the electrode spacing, and the third character after the second underscore indicates the polarity of the voltage sweep.

P (mW)	A_5_N	A_5_P	A_7.5_N	A_7.5_P
5	2, 000	1, 000	2, 000	2, 000
10	2, 000	1, 000	1, 000	1, 000
20	3, 000	1, 000	1, 000	1, 000
30	2, 000	1, 000	1, 000	1, 000
40	2, 000	1, 000	2, 000	1, 000

Table S2. Effective Schottky barrier height Φ_B values in eV, calculated according equation (8), for all negative and positive voltage sweeps at every optical power of every measured electrode pair of sample A. The first character before the first underscore indicates the sample, the second character between the underscores indicates the electrode spacing, and the third character after the second underscore indicates the polarity of the voltage sweep.

P (mW)	A_5_N	A_5_P	A_7.5_N	A_7.5_P
5	0.10	0.12	0.11	0.13
10	0.08	0.10	0.10	0.11
20	0.02	0.06	0.09	0.09
30	-0.02	0.02	0.06	0.07
40	-0.03	0.00	0.03	0.05

Table S3. Effective Schottky barrier height Φ_B values in eV, calculated according equation (6), for all negative and positive voltage sweeps at every optical power of every measured electrode pair of sample A. The first character before the first underscore indicates the sample, the second character between the underscores indicates the electrode spacing, and the third character after the second underscore indicates the polarity of the voltage sweep.

P (mW)	A_5_N	A_5_P	A_7.5_N	A_7.5_P
5	-800	-100, 000	-1, 000	-100
10	-800	-200	-700	-20
20	-1, 000, 000	-100, 000	-700	-300
30	-1, 000	-200	-700	-100
40	-700	-100	-900	-40, 000

Table S4. Tunneling parameter E_0 values in eV, calculated according equation (4), for all negative and positive voltage sweeps at every optical power of every measured electrode pair of sample A. The first character before the first underscore indicates the sample, the second character between the underscores indicates the electrode spacing, and the third character after the second underscore indicates the polarity of the voltage sweep.

P (mW)	A_5_N	A_5_P	A_7.5_N	A_7.5_P
5	40.70	34.29	40.60	39.58
10	42.54	30.28	37.98	37.75
20	83.84	29.46	34.83	35.12
30	63.01	30.63	37.21	34.26
40	57.00	35.32	50.50	32.54

Table S5. Tunneling parameter E_0 values in eV, calculated according equation (7), for all negative and positive voltage sweeps at every optical power of every measured electrode pair of sample A. The first character before the first underscore indicates the sample, the second character between the underscores indicates the electrode spacing, and the third character after the second underscore indicates the polarity of the voltage sweep.

P (mW)	A_5_N	A_5_P	A_7.5_N	A_7.5_P
5	50	6, 000	60	9
10	50	20	40	2
20	40, 000	5, 000	40	20
30	60	10	40	8
40	40	7	50	2, 000

Table S6. I_{sat} values in nA for all negative and positive voltage sweeps at every optical power of every measured electrode pair of sample B. The first character before the first underscore indicates the sample, the second character between the underscores indicates the electrode spacing, and the third character after the second underscore indicates the polarity of the voltage sweep.

P (mW)	B_5_N	B_5_P	B_15_N	B_15_P
5	13.08	n/a	8, 031.55	n/a
10	0.95	1.66	12.15	n/a
20	4.96	10.80	56.76	n/a
30	18.17	n/a	66.03	n/a
40	9.31	54.31	88.95	n/a

Table S7. Voltage window V values in V, over which te photocurrent transitions to saturation, for all negative and positive voltage sweeps at every optical power of every measured electrode pair of sample B. The first character before the first underscore indicates the sample, the second character between the underscores indicates the electrode spacing, and the third character after the second underscore indicates the polarity of the voltage sweep.

P (mW)	B_5_N	B_5_P	B_15_N	B_15_P
5	44.20	n/a	100	n/a
10	0.18	0.33	33.86	n/a
20	0.53	2.43	35.70	n/a
30	19.82	n/a	28.54	n/a
40	1.70	1.82	40.62	n/a

Table S8. g_n values in $cm^{-3}s^{-1}$ for all negative and positive voltage sweeps at every optical power of every measured electrode pair of sample B. The first character before the first underscore indicates the sample, the second character between the underscores indicates the electrode spacing, and the third character after the second underscore indicates the polarity of the voltage sweep.

P (mW)	B_5_N	B_5_P	B_15_N	B_15_P
5	$1.63x10^{11}$	n/a	$3.34x10^{13}$	n/a
10	$1.19x10^{10}$	$2.08x10^{10}$	$5.06x10^{10}$	n/a
20	$6.19x10^{10}$	$1.35x10^{11}$	$2.36x10^{11}$	n/a
30	$2.27x10^{11}$	n/a	$2.75x10^{11}$	n/a
40	$1.16x10^{11}$	$6.78x10^{11}$	$3.70x10^{11}$	n/a

Table S9. τ_n values in μs for all negative and positive voltage sweeps at every optical power of every measured electrode pair of sample B. The first character before the first underscore indicates the sample, the second character between the underscores indicates the electrode spacing, and the third character after the second underscore indicates the polarity of the voltage sweep.

P (mW)	B_5_N	B_5_P	B_15_N	B_15_P
5	0.03	n/a	0.00	n/a
10	7.89	4.22	0.12	n/a
20	2.61	0.57	0.12	n/a
30	0.07	n/a	0.15	n/a
40	0.82	0.76	0.10	n/a

Table S10. T_c values in K for all negative and positive voltage sweeps at every optical power of every measured electrode pair of sample B. The first character before the first underscore indicates the sample, the second character between the underscores indicates the electrode spacing, and the third character after the second underscore indicates the polarity of the voltage sweep.

P (mW)	B_5_N	B_5_P	B_15_N	B_15_P
5	n/a	504	n/a	192
10	n/a	n/a	n/a	273
20	n/a	n/a	n/a	657
30	n/a	nan	n/a	660
40	n/a	n/a	n/a	501

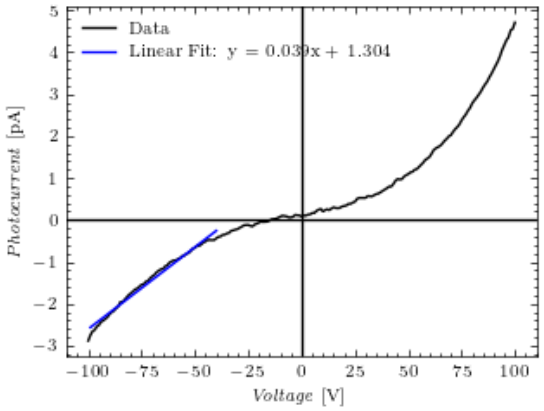

(a)

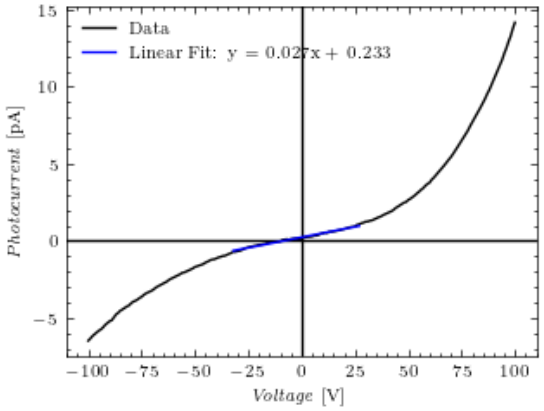

(b)

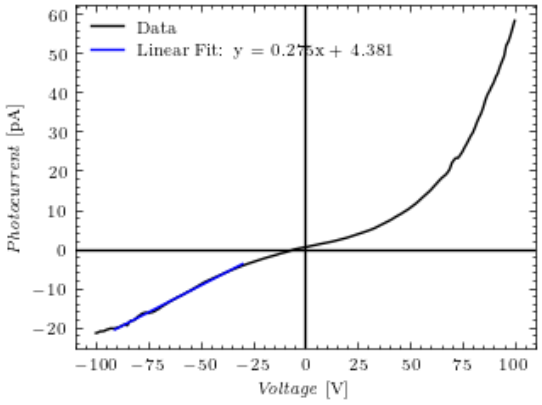

(c)

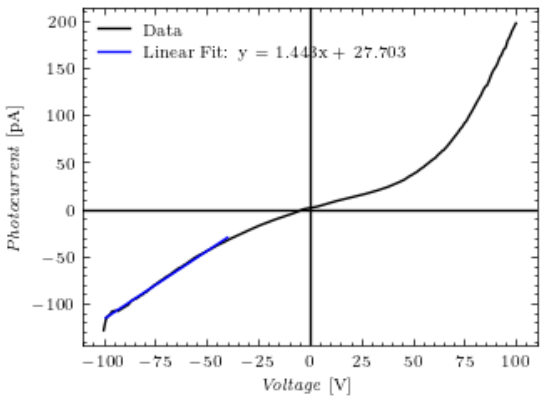

(d)

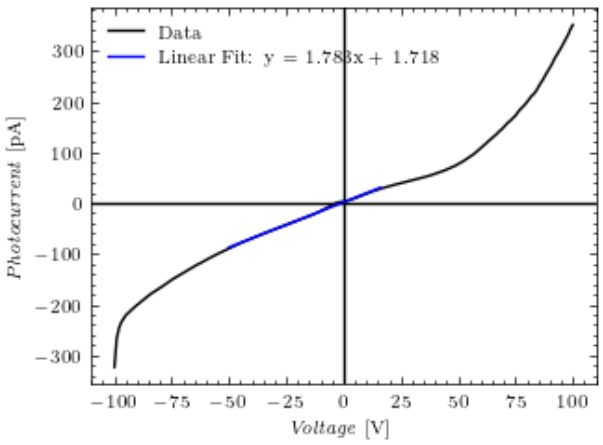

(e)

Figure S5. Linear fits of the *I-V* characteristics of sample A at an electrode spacing of 5 μm with an R^2 of 0.97 at an optical power of a) 5 mW, b) 10 mW, c) 20 mW, d) 30 mW and e) 40 mW.

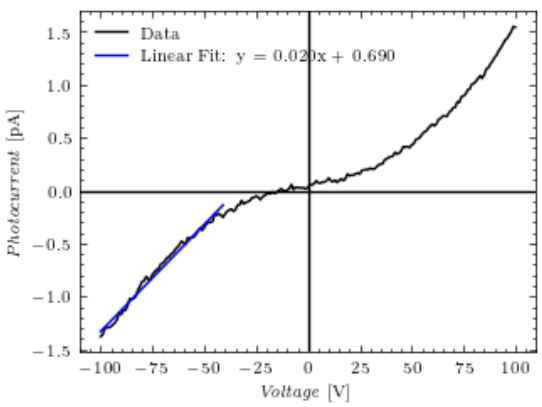

(a)

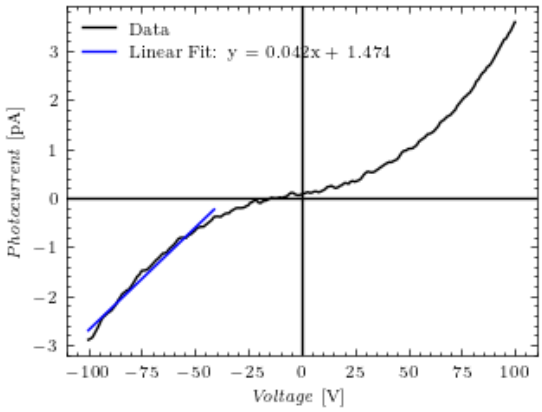

(b)

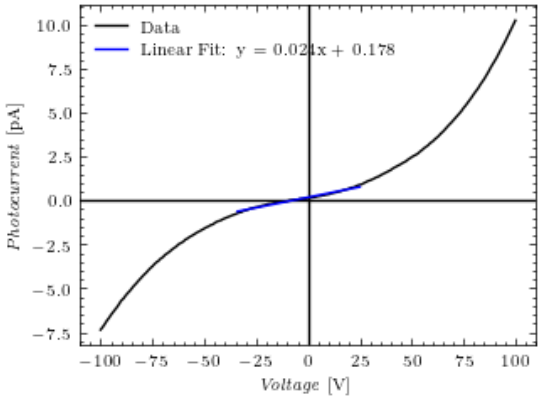

(c)

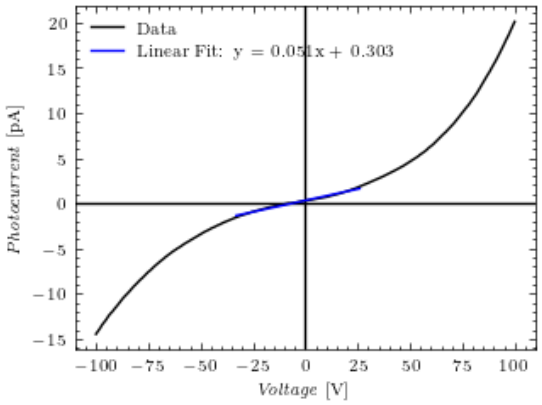

(d)

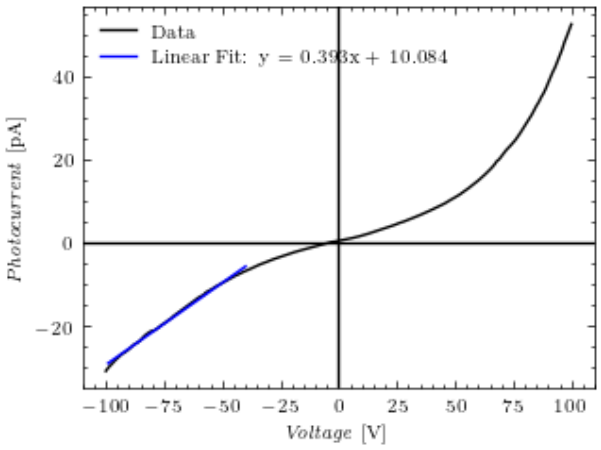

(e)

Figure S6. Linear fits of the *I-V* characteristics of sample A at an electrode spacing of 7.5 μm with an R^2 of 0.97 at an optical power of a) 5 mW, b) 10 mW, c) 20 mW, d) 30 mW and e) 40 mW.

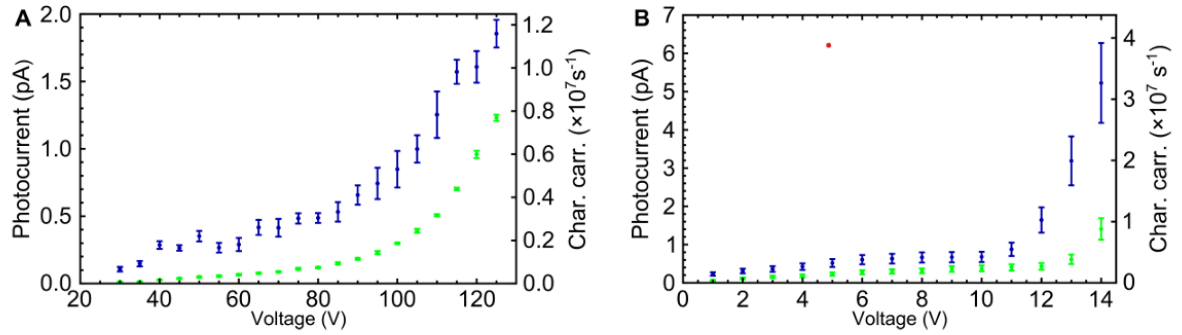

Fig. S3.

Photocurrent as a function of applied voltage. (**A**) and (**B**) photocurrent-voltage characteristics obtained for single NV centers embedded in commercial sample a and in-house grown sample c, respectively. Blue data points show signal from single center, while green data points show background photocurrent.

Figure S7. Screenshot of supplementary figure 'Fig. S3.' of Siyushev et al.[14] presenting an *I-V* characteristic of a conventional Ti PDMR electrode configuration.

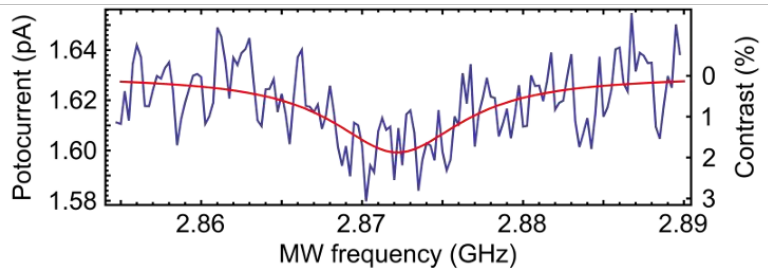

Fig. S5.

PDMR signal. The PDMR signal obtained on a single NV center in continuous wave mode, so that the frequency of the microwave field is swept while defect is constantly illuminated with laser light. The contrast is estimated from the Lorentzian fit.

Figure S8. Screenshot of supplementary figure 'Fig. S5.' of Siyushev et al.[14] used in the calculation of EQE_{2P}.

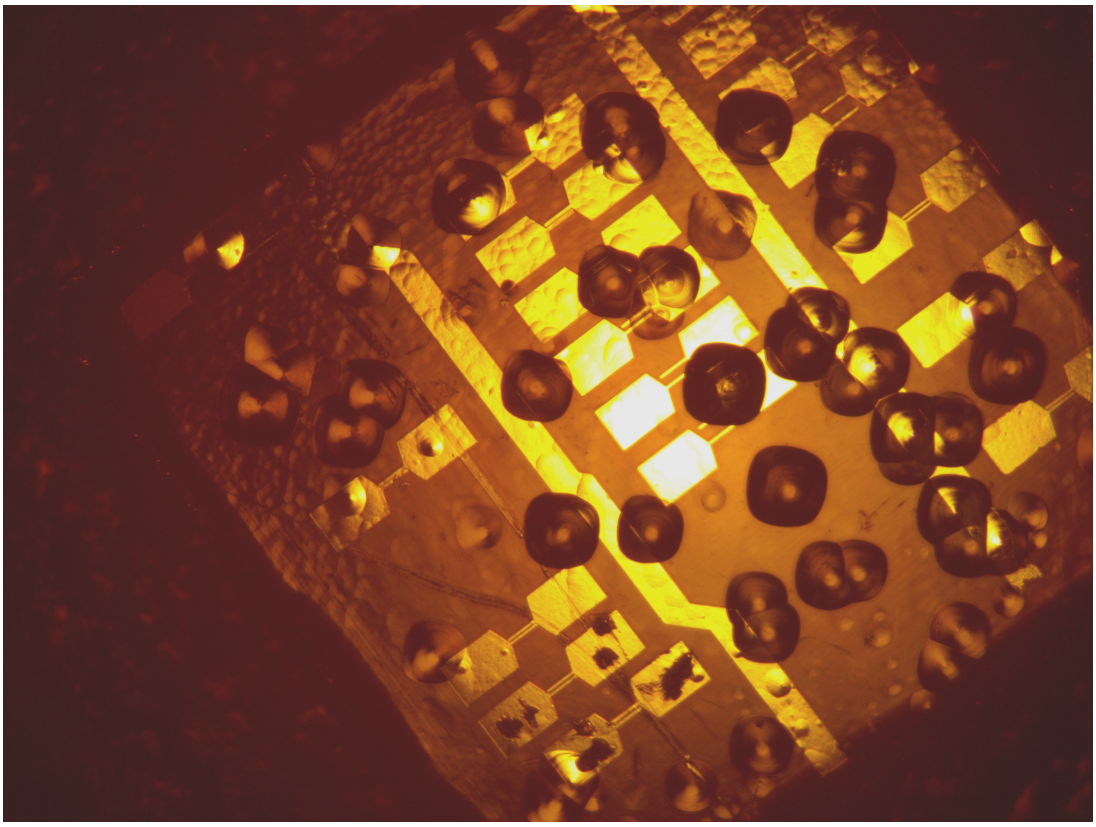

Figure S9. Microscope image of sample A after RIE with oxygen plasma.

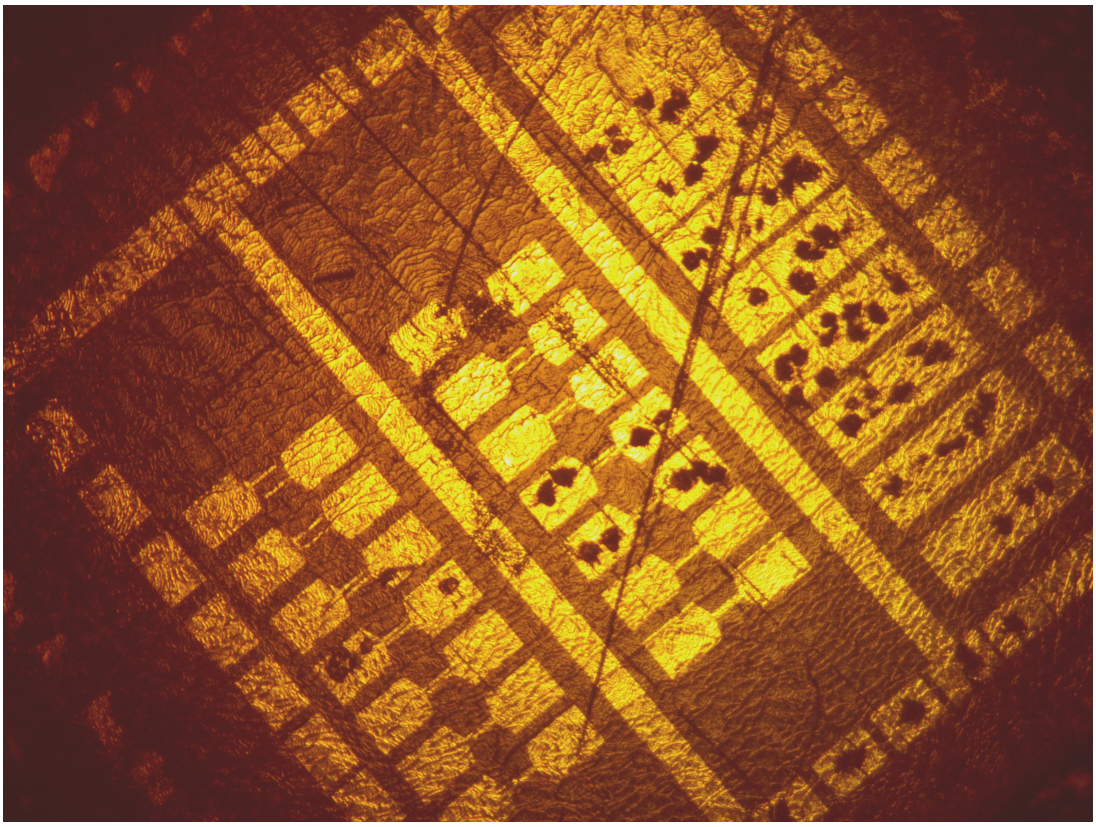

Figure S10. Microscope image of sample B after RIE with oxygen plasma.

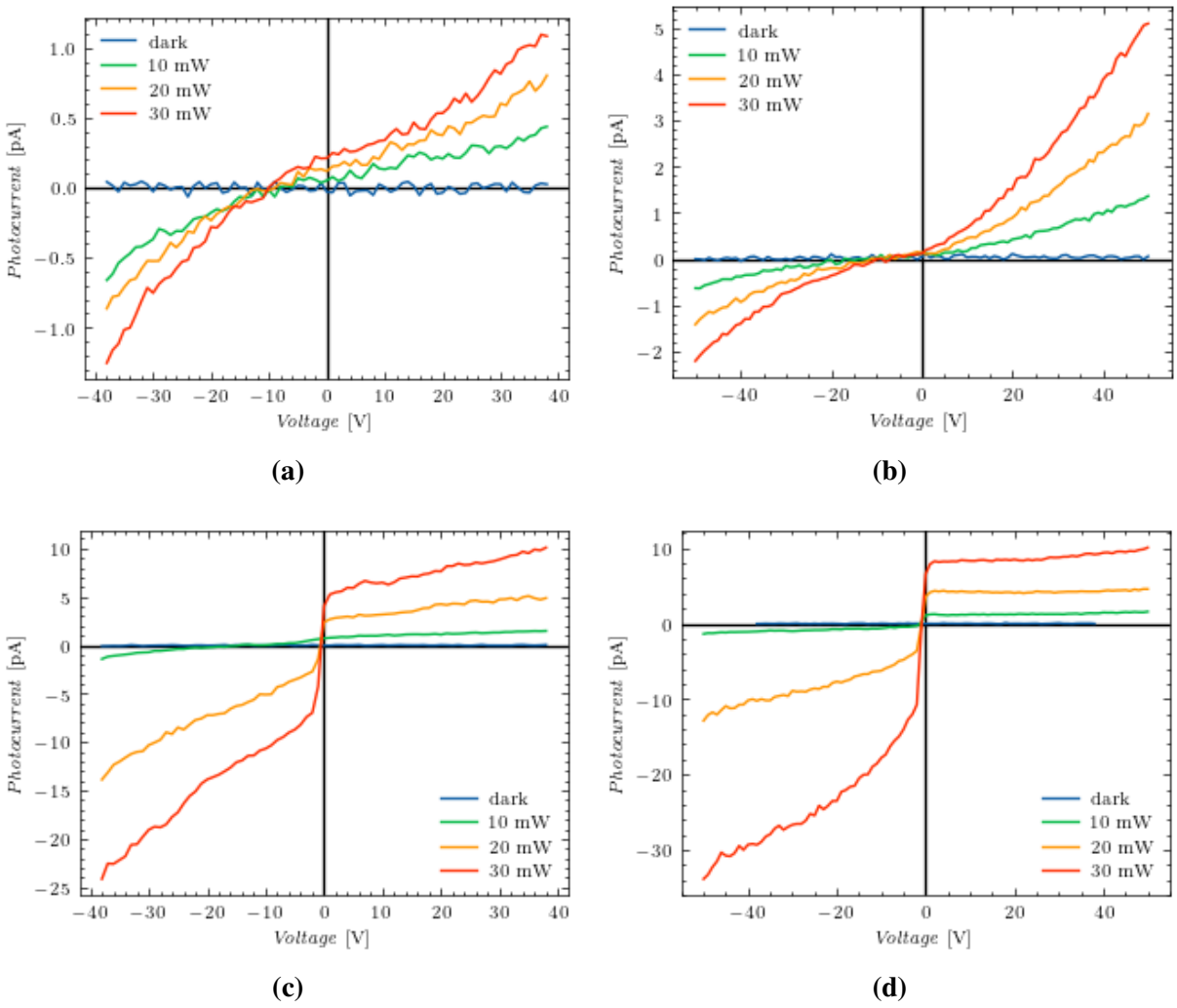

Figure S11. Initial measured *I-V* characteristics at different optical powers by dr. E. Bourgeois for a) sample A with an electrode spacing of 7.5 μm, b) sample A with an electrode spacing of 10 μm, c) sample B with an electrode spacing of 7.5 μm and d) sample B with an electrode spacing of 10 μm.